

Localized interlayer complexes in heterobilayer transition metal dichalcogenides

M. Danovich, D. A. Ruiz-Tijerina and V. I. Fal'ko

*National Graphene Institute, University of Manchester,
Booth St E, Manchester M13 9PL, United Kingdom*

R. J. Hunt, M. Szyniszewski, and N. D. Drummond

Department of Physics, Lancaster University, Lancaster LA1 4YB, United Kingdom

(Dated: December 3, 2024)

We present theoretical results for the radiative rates and doping-dependent photoluminescence spectrum of interlayer excitonic complexes localized by donor impurities in $\text{MoSe}_2/\text{WSe}_2$ twisted heterobilayers, supported by quantum Monte Carlo calculations of binding energies and wave-function overlap integrals. For closely aligned layers, radiative decay is made possible by the momentum spread of the localized complexes' wave functions, resulting in few μs^{-1} radiative rates. For strongly misaligned layers, the short-range interaction between the carriers and impurity provides a finite radiative rate with a strong asymptotic twist angle dependence $\propto \theta^{-8}$. Finally, phonon-assisted recombination is considered, with emission of optical phonons in both layers resulting in additional weaker emission lines, red-shifted by the phonon energy.

I. INTRODUCTION

Recent advances in the study of two-dimensional (2D) materials have allowed the realization of van der Waals (vdW) heterostructures consisting of vertically stacked 2D layers, resulting in unique properties and potential novel device applications [1–5]. The layers forming these heterostructures are only weakly bound by vdW forces, and largely retain their individual characteristic properties. Yet, the weak interlayer coupling allows the different properties of various 2D materials to be combined.

One such family of vdW heterostructures are heterobilayers of 2D transition metal dichalcogenides (TMDs), which have attracted much interest due to their unique optical properties, dominated by strongly bound excitonic complexes [6, 7] and spin- and valley-dependent optical selection rules [8, 9]. The most commonly studied heterobilayers are of the form MoX_2/WX_2 , with $\text{X} = \text{S}$ or Se , due to their type-II (staggered) band alignment, in which the lowest conduction band (CB) edge and the highest valence band (VB) edge are spatially confined to different layers [10, 11]. In this configuration, electrostatic interactions between electrons and holes across the heterostructure result in the formation of interlayer excitonic complexes, whose constituent carriers are spatially separated in the out-of-plane direction. Optical signatures of these interlayer complexes have been reported in photoluminescence (PL) experiments [12–14], where new PL peaks are observed in the spectra of bilayer regions. These signatures appear at energies below the monolayer photoemission lines, due to the smaller interlayer band gap in the staggered band configuration.

Photoemission by free interlayer excitons is limited by the relative interlayer angle θ and the incommensurability of the two TMD lattices δ , resulting in a momentum-space mismatch $\Delta K \approx K\sqrt{\delta^2 + \theta^2}$ between the conduction- and valence-band edges, as shown in Fig. 2(b). Radiative recombination becomes effectively indirect, and thus suppressed by energy and momentum conservation [15]. These constraints are relaxed when interlayer excitons and larger excitonic complexes local-

ize about charged defects, such as donor ions, which are commonly observed as dopants in real samples. Formation of these complexes is favored by the long interlayer exciton lifetimes resulting from the spatial separation of their carriers, which allow for their localization by the deep potential wells provided by the ions. The spread in momentum space of these localized complexes opens the possibility for a finite radiative matrix element $M \propto \int d^2r e^{i\Delta\mathbf{K}\cdot\mathbf{r}}\Psi(\mathbf{r})$, where $\Psi(\mathbf{r})$ is the envelope wave function of the complex.

In this paper, we provide a theory for the radiative recombination of localized interlayer complexes in TMD heterostructures of the form MoX_2/WX_2 , where the carriers are bound to a donor ion in the MoX_2 layer. Focusing specifically on $\text{MoSe}_2/\text{WSe}_2$, we use variational and diffusion quantum Monte Carlo (VMC and DMC) simulations [16, 17] to evaluate the binding energies and wave-function overlap integrals of complexes involving a single hole in the WSe_2 layer and up to three electrons in the MoSe_2 layer, accounting for bilayer and encapsulation screening effects.

Motivated by the binding energies obtained from our quantum Monte Carlo (QMC) calculations and PL experiments [18], we study the radiative recombination of the two simplest such complexes consisting of MoX_2 electrons and a single WX_2 hole bound to an impurity center: a donor ion and an exciton ($D_c^0 h_v$), and a donor-bound trion ($D_c^0 X_{vc'}$). We predict the PL spectrum from these complexes for well-aligned TMD heterobilayers, and estimate the asymptotic behavior of their PL signals in the regime of strong misalignment based on a perturbative analysis. Our results indicate a rapid decay of the PL signals from the most relevant donor-bound interlayer complexes with the interlayer twist angle (θ), resulting from the asymptotic behavior $\Gamma \sim \theta^{-8}$ of the radiative rates at strong misalignment. As a consequence, we expect that optical signatures from these complexes can be detected only in closely aligned crystals.

The remainder of this paper is organized as follows. In Sec. II we discuss the model Hamiltonian for the TMD heterobilayer, describe our approach to calculating its op-

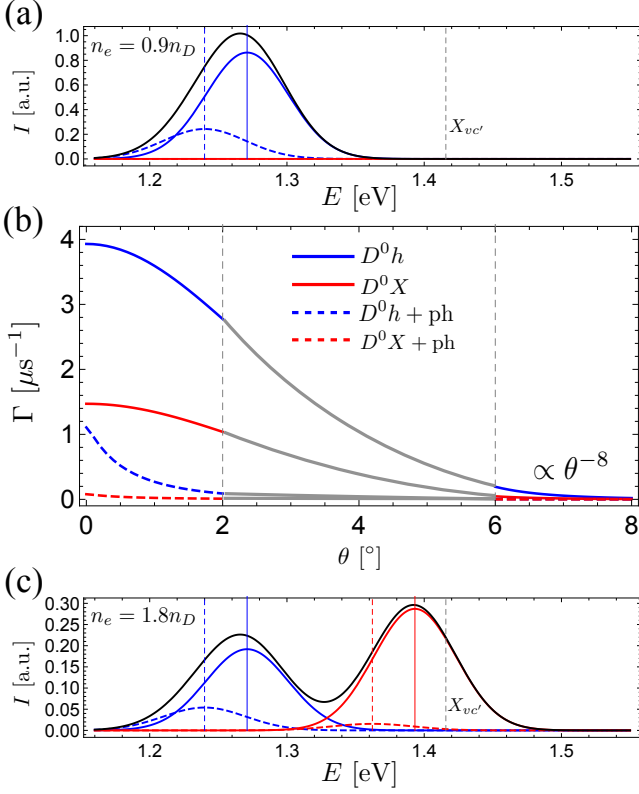


FIG. 1. (a) Simulated PL spectrum of donor-bound interlayer complexes in an aligned ($\theta = 0$) MoSe₂/WSe₂ bilayer encapsulated in hBN, for an electron density of $n_e = 0.9n_D$, with n_D the donor density. Dashed lines indicate PL from phonon-assisted recombination. The lines are taken to have Gaussian shape with width $2\sigma = 60$ meV, and the interlayer gap is $\bar{E}_g = 1.5$ eV. The vertical gray dashed line in (a) and (c) indicates the position of the free interlayer exciton $X_{vc'}$. (b) Radiative rates of the $D_c^0h_v$ (per hole) (solid blue) and $D_c^0X_{vc'}$ (solid red) complexes, and their phonon-assisted replicas (dashed), in the large and small twist angle (θ) limits. The rates have a strong angular dependence, with asymptotic behaviour $\sim \theta^{-8}$ for radiative decay driven by short-range interactions, and $\sim \theta^{-4}$ for phonon-assisted processes. The gray lines for intermediate twist angles $\theta = 2 - 6^\circ$ have been interpolated by hand. (c) Simulated PL spectrum in the limit of heavy n-doping, showing the appearance of the donor-bound trion ($D_c^0X_{vc'}$) line when $n_e > n_D$. Parameters: $n_h = 10^{11}$ cm⁻² and $n_D = 10^{13}$ cm⁻².

tical properties, and present our DMC results for the binding energies of the main interlayer impurity-bound complexes. In Sec. III we address the PL signatures of these complexes, assuming good alignment between the TMD monolayers in the heterostructure, and estimate the asymptotic behavior of their radiative decay with twist angle in Sec. IV. We consider the effects of electron-phonon interactions in Sec. V, and we find that longitudinal optical phonon modes can introduce red-shifted replicas to the main PL lines. Finally, we estimate the evolution of the PL spectrum of the two main donor-bound interlayer complexes with doping in Sec. VI. Our conclusions are summarized in Fig. 1, and discussed in Sec. VII.

II. MODEL

A. Electrostatic interactions in a bilayer system

The reduced dimensionality of a monolayer TMD leads to modified electrostatic interactions between its charge carriers below a characteristic length scale $r_* = 2\pi\kappa/\epsilon$ (in Gaussian units), determined by the monolayer's in-plane dielectric susceptibility κ , and the (average) dielectric constant ϵ of its environment [19, 20]. In a TMD heterobilayer, further screening effects must be considered. The resulting interactions between same-layer carriers \mathcal{V} in one layer and \mathcal{V}' in the other, and the interlayer interaction \mathcal{W} , have Fourier components (Appendix A)

$$\mathcal{V}(\mathbf{q}) = \frac{2\pi (1 + r'_* q - r'_* q e^{-2qd})}{\epsilon q [(1 + r_* q)(1 + r'_* q) - r_* r'_* q^2 e^{-2qd}]}, \quad (1a)$$

$$\mathcal{V}'(\mathbf{q}) = \frac{2\pi (1 + r_* q - r_* q e^{-2qd})}{\epsilon q [(1 + r_* q)(1 + r'_* q) - r_* r'_* q^2 e^{-2qd}]}, \quad (1b)$$

$$\mathcal{W}(\mathbf{q}) = \frac{2\pi e^{-qd}}{\epsilon q [(1 + r_* q)(1 + r'_* q) - r_* r'_* q^2 e^{-2qd}]}, \quad (1c)$$

where \mathbf{q} is the wave vector, $d \ll r_*, r'_*$ is the interlayer distance, and r_* and r'_* are the corresponding monolayer screening lengths.

Previous works on monolayer TMDs have focused on interactions of the Keldysh form [19] to study their excitonic spectra and optical properties [6, 20–23]. For bilayers, this potential form is obtained from Eqs. (1a)–(1c) in the long-range limit ($q \ll 1/r_*, 1/r'_*$) as

$$\mathcal{V}_<(\mathbf{q}) = \mathcal{V}'_<(\mathbf{q}) = \frac{2\pi}{\epsilon q [1 + (r_* + r'_*)q]}, \quad (2a)$$

$$\mathcal{W}_<(\mathbf{q}) = \frac{2\pi}{\epsilon q [1 + (r_* + r'_* + d)q]}. \quad (2b)$$

By contrast, in the short-range limit ($q \gg 1/r_*, 1/r'_*$) we obtain for the intralayer interactions

$$\mathcal{V}_>(\mathbf{q}) = \frac{2\pi}{\epsilon r_* q^2}, \quad \mathcal{V}'_>(\mathbf{q}) = \frac{2\pi}{\epsilon r'_* q^2}, \quad (3)$$

revealing the absence of screening from the opposite layer in this regime. More strikingly, the short-range interlayer potential vanishes exponentially as $\mathcal{W}_>(\mathbf{q}) = 2\pi e^{-qd}/(\epsilon r_* r'_* q^3)$. Neither of these features is captured by extrapolation of Eqs. (2a) and (2b) to large wave numbers.

B. Photon emission by donor-bound complexes

As in the monolayer case [24–27], optical properties of the heterobilayer are determined by excitonic complexes formed by excess electrons and holes in the sample. Staggered (type-II) band alignment, in which the

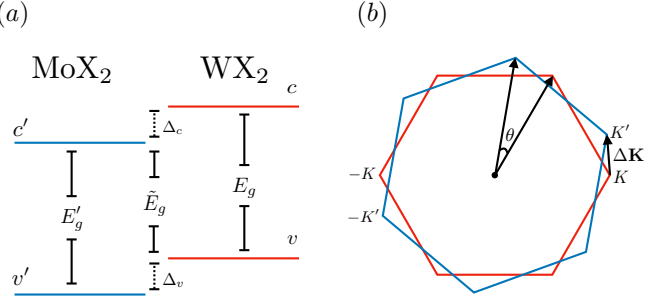


FIG. 2. (a) Schematic of type-II band alignment in a TMD heterobilayer. The CB and VB of the two layers are shifted relative to each other by energies Δ_c and Δ_v , respectively, giving an interlayer gap of \tilde{E}_g . (b) The Brillouin zones (BZs) of the misaligned TMD monolayers. Their K valleys are separated by a momentum vector $\Delta\mathbf{K}$, due to the nonzero misalignment angle θ and to the difference in lattice constants.

main electron and hole bands belong to opposite layers, is typical of TMD heterostructures [10]. This is shown schematically in Fig. 2(a) for a MoX₂/WX₂ structure, where X = S or Se represents a chalcogen; the electron and hole bands are labeled c' and v , respectively, and the primed (unprimed) band labels correspond to the MoX₂ (WX₂) layer. Given the reduced band gap \tilde{E}_g [Fig. 2(a)], the lowest-energy exciton states are spread across the heterostructure, formed by c' -band electrons and v -band holes bound by the interaction $\mathcal{W}(\mathbf{q})$ [12, 13, 28].

The optical activity of interlayer excitons in TMD bilayers is strongly constrained by the interlayer alignment. As shown in Fig. 2(b), the relative twist angle and lattice incommensurability between the two layers produces a mismatch between their Brillouin zones (BZs). Thus, bright interlayer excitons in MoX₂/WX₂ structures, consisting of same-valley c' -band electrons and v -band holes, have a finite center-of-mass momentum $\Delta\mathbf{K} = \mathbf{K}' - \mathbf{K}$. Due to energy and momentum conservation, photon emission by interlayer excitons is only allowed when $\Delta K \approx 0$ [29].

The above restrictions are relaxed when excitons, and other excitonic complexes are bound to impurity centers in the sample, such as charged defects and donor ions. These complexes are localized within some characteristic length a_0^* , known as the exciton Bohr radius, such that their momentum-space wave functions are finite up to momenta of order $1/a_0^*$. As a result, the recombination rates of impurity-bound interlayer complexes are determined by the large-momentum tail of their wave function, and thus by the short-range interaction (3).

The Hamiltonian for the heterobilayer in the free-

carrier basis is

$$\hat{H} = \hat{H}_0 + \hat{H}_t + \hat{U}_{\text{intra}} + \hat{U}_{\text{inter}}, \quad (4)$$

where the zeroth-order Hamiltonian \hat{H}_0 , describing the CB and VB electrons of the two individual layers, is given in second quantization as

$$\hat{H}_0 = \sum_{\alpha} \sum_{\mathbf{k}, \tau, \sigma} E_{\alpha}(\mathbf{k}) c_{\alpha, \tau, \sigma}^{\dagger}(\mathbf{k}) c_{\alpha, \tau, \sigma}(\mathbf{k}). \quad (5)$$

$c_{\alpha, \tau, \sigma}^{\dagger}(\mathbf{k})$ creates an electron of spin projection $\sigma = \uparrow, \downarrow$ and momentum \mathbf{k} relative to the $\tau\mathbf{K}$ valley ($\tau = \pm$) of band $\alpha = c', v', c, v$. The band dispersions are

$$E_{v'}(\mathbf{k}) = -\Delta_v - \frac{\hbar^2 k^2}{2m'_v}, \quad (6a)$$

$$E_v(\mathbf{k}) = -\frac{\hbar^2 k^2}{2m_v}, \quad (6b)$$

$$E_{c'}(\mathbf{k}) = \tilde{E}_g + \frac{\hbar^2 k^2}{2m'_{c'}}, \quad (6c)$$

$$E_c(\mathbf{k}) = \tilde{E}_g + \Delta_c + \frac{\hbar^2 k^2}{2m_c}, \quad (6d)$$

where Δ_c (Δ_v) is the spacing between the electron (hole) band edges [Fig. 2(a)].

The tunnelling Hamiltonian describing electron hopping between the layers is given by

$$\begin{aligned} \hat{H}_t = & \sum_{\tau, \sigma} \sum_{\mathbf{G}, \mathbf{G}', \mathbf{k}, \mathbf{k}'} \delta_{\tau\mathbf{K} + \mathbf{k} + \mathbf{G}, \tau'\mathbf{K}' + \mathbf{k}' + \mathbf{G}'} \\ & \times \left\{ [t_{cc}(\mathbf{k} + \mathbf{K} + \mathbf{G}) c_{c\tau\sigma}^{\dagger}(\mathbf{k}) c_{c'\tau'\sigma}(\mathbf{k}') \right. \\ & \left. + t_{vv}(\mathbf{k} + \mathbf{K} + \mathbf{G}) c_{v\tau\sigma}^{\dagger}(\mathbf{k}) c_{v'\tau'\sigma}(\mathbf{k}')] + \text{H.c.} \right\}, \end{aligned} \quad (7)$$

where $t_{cc}(\mathbf{k})$ and $t_{vv}(\mathbf{k})$ are stacking-dependent interlayer hopping strengths between the CBs and VBs; \mathbf{G} and \mathbf{G}' correspond to the reciprocal lattice vectors in the hole and electron layers; and the Kronecker delta enforces momentum conservation in the tunnelling process [30, 31]. We focus on configurations close to AA stacking, and use the hopping terms $t_{\alpha\alpha}(\mathbf{k})$ reported in Ref. [31]. These values are small (few meV) compared to all other scales in the problem, reflecting the vdW and electrical quadrupole nature of the interlayer interactions. As a result, \hat{H}_t can be treated within perturbation theory. Furthermore, since $t_{\alpha\alpha}(\mathbf{k})$ decay rapidly with k [31], we truncate the sums over \mathbf{G} and \mathbf{G}' to only the first nonzero vectors, and set $t_{cc}(\mathbf{k}) \approx t_{cc} = 2.5$ meV and $t_{vv}(\mathbf{k}) \approx t_{vv} = 16$ meV.

Finally, the direct electrostatic interactions between carriers, and between carriers and a positive donor ion of effective charge Z_{donor} , are given by

$$\begin{aligned} \hat{U}_{\text{intra}} = & \frac{e^2}{S} \sum_{\substack{\tau_1, \tau_2 \\ \sigma_1, \sigma_2}} \sum_{\mathbf{k}_1, \mathbf{k}_2, \xi} \left[\sum_{\alpha, \beta=v, c} \frac{\mathcal{V}(\xi)}{(1 + \delta_{\alpha, \beta})} c_{\alpha, \tau_1, \sigma_1}^\dagger(\mathbf{k}_1 + \xi) c_{\beta, \tau_2, \sigma_2}^\dagger(\mathbf{k}_2 - \xi) c_{\beta, \tau_2, \sigma_2}(\mathbf{k}_2) c_{\alpha, \tau_1, \sigma_1}(\mathbf{k}_1) \right. \\ & \left. + \sum_{\alpha, \beta=v', c'} \frac{\mathcal{V}(\xi)}{(1 + \delta_{\alpha, \beta})} c_{\alpha, \tau_1, \sigma_1}^\dagger(\mathbf{k}_1 + \xi) c_{\beta, \tau_2, \sigma_2}^\dagger(\mathbf{k}_2 - \xi) c_{\beta, \tau_2, \sigma_2}(\mathbf{k}_2) c_{\alpha, \tau_1, \sigma_1}(\mathbf{k}_1) \right] \\ & - \frac{Z_{\text{donor}} e^2}{S} \sum_{\tau, \sigma} \sum_{\mathbf{k}, \xi} \sum_{\alpha=v', c'} \mathcal{V}'(\xi) c_{\alpha, \tau, \sigma}^\dagger(\mathbf{k} + \xi) c_{\alpha, \tau, \sigma}(\mathbf{k}), \end{aligned} \quad (8a)$$

$$\begin{aligned} \hat{U}_{\text{inter}} = & \frac{e^2}{S} \sum_{\substack{\tau_1, \tau_2 \\ \sigma_1, \sigma_2}} \sum_{\mathbf{k}_1, \mathbf{k}_2, \xi} \sum_{\alpha=v, c} \sum_{\beta=v', c'} \mathcal{W}(\xi) c_{\alpha, \tau_1, \sigma_1}^\dagger(\mathbf{k}_1 + \xi) c_{\beta, \tau_2, \sigma_2}^\dagger(\mathbf{k}_2 - \xi) c_{\beta, \tau_2, \sigma_2}(\mathbf{k}_2) c_{\alpha, \tau_1, \sigma_1}(\mathbf{k}_1) \\ & - \frac{Z_{\text{donor}} e^2}{S} \sum_{\tau, \sigma} \sum_{\mathbf{k}, \xi} \sum_{\alpha=v, c} \mathcal{W}(\xi) c_{\alpha, \tau, \sigma}^\dagger(\mathbf{k} + \xi) c_{\alpha, \tau, \sigma}(\mathbf{k}), \end{aligned} \quad (8b)$$

where ξ is the momentum transfer, and S the sample area. The donor ion is treated as a dispersionless scatterer, and is assumed to be present in the MoX_2 (electron) layer. Henceforth, we assume that a donor yields a single electron to the TMD and set $Z_{\text{donor}} = 1$.

The radiative recombination of electrons and holes is driven by the light-matter interaction

$$\hat{H}_{\text{r}} = \frac{e\gamma}{\hbar c} \sum_{\mathbf{q}} \sum_{\mathbf{k}, \tau, \sigma} \sqrt{\frac{4\pi\hbar c}{Vq}} c_{v, \tau, \sigma}^\dagger(\mathbf{k} - \mathbf{q}_{\parallel}) c_{c, \tau, \sigma}(\mathbf{k}) a_{\tau}^\dagger(\mathbf{q}), \quad (9)$$

in the WX_2 layer and an analogous term \hat{H}'_{r} in the MoX_2 layer. Here, $\gamma^{(\prime)}$ is given by the in-plane momentum matrix element between $c^{(\prime)}$ and $v^{(\prime)}$ band states, evaluated at the $\pm K$ points of the BZ [32]. $a_{\tau}^\dagger(\mathbf{q})$ creates a photon of momentum \mathbf{q} and in-plane polarization τ , determined by the electron's valley degree of freedom, where $\tau = +$ ($\tau = -$) represents right-handed (left-handed) circular polarization. The photon momentum $\mathbf{q} = \mathbf{q}_{\parallel} + \mathbf{q}_{\perp}$ is split into its in-plane and out-of-plane components, respectively, and $V = SL$, with L the height of the optical cavity.

Let $|\Psi\rangle$ be an interlayer excitonic eigenstate of the Hamiltonian $\hat{H}_0 + \hat{U}_{\text{intra}} + \hat{U}_{\text{inter}}$ of energy E_{Ψ} . Photon emission through the term \hat{H}_{r} requires the recombining carriers to be in the same TMD layer. This is allowed by the perturbation \hat{H}_{t} , giving the first-order correction to the wave function

$$|\Psi^{(1)}\rangle = \sum_n \frac{\langle n | \hat{H}_{\text{t}} | \Psi \rangle}{E_n - E_{\Psi}} |n\rangle, \quad (10)$$

where the sum runs over the eigenstates $|n\rangle$ of $\hat{H}_0 + \hat{U}_{\text{intra}} + \hat{U}_{\text{inter}}$, with energies E_n . The resulting rate of radiative recombination is then given by Fermi's golden rule as

$$\Gamma_{\Psi} = \frac{2\pi}{\hbar} \sum_f \left| \langle f | [\hat{H}_{\text{r}} + \hat{H}'_{\text{r}}] | \Psi^{(1)} \rangle \right|^2 \delta(E_f - E_{\Psi}), \quad (11)$$

where $\{ |f \rangle \}$ is the set of possible final states, containing one additional photon. As discussed below, the relevant matrix elements in Eq. (11) can be evaluated numerically in QMC.

III. RECOMBINATION OF DONOR-BOUND INTERLAYER COMPLEXES

A. Model parameters

We now discuss the optical emission signatures of the most relevant donor-bound interlayer excitonic complexes predicted by VMC and DMC simulations. For concreteness, we will focus on $\text{MoSe}_2/\text{WSe}_2$ heterobilayers (X=Se); parameters relevant to this pair of materials are shown in Table I. Furthermore, we assume that the heterobilayer is encapsulated in bulk hBN, and set the dielectric constant to $\epsilon = 4$. Our chosen value of 4 corresponds to the high-frequency dielectric constant of hBN, which is reasonable as the exciton binding energy is considerably larger than the highest optical phonon frequency of hBN. The tensor nature of the hBN dielectric constant supplies an effective dielectric constant $\bar{\epsilon} = \sqrt{\epsilon_{\parallel} \epsilon_{\perp}}$ and renormalizes the interlayer distance d by a factor $\sqrt{\epsilon_{\parallel} / \epsilon_{\perp}}$, where ϵ_{\parallel} and ϵ_{\perp} are the in-plane and out-of-plane dielectric constants (see Appendix A). However, taking $\epsilon_{\parallel}(\infty)$ and $\epsilon_{\perp}(\infty)$ from various sources we find that $3.1 < \sqrt{\epsilon_{\parallel} \epsilon_{\perp}} < 4.5$ and $0.71 < \sqrt{\epsilon_{\parallel} / \epsilon_{\perp}} < 0.95$ [33–36]. This justifies, in part, our use of $\epsilon = 4$ and our use of the physical layer separation, but as a check of the robustness of our results, we have considered a few other dielectric environments for a restricted set of charge complexes.

The Hamiltonian Eq. (4), without \hat{H}_{t} (or, with charges being fixed in their layers), was solved using DMC, for various numbers of excess electrons and holes, and in the presence of donor impurities in the MoSe_2 layer. Our DMC total energies are statistically exact: we have considered no complexes containing any pairs of indistin-

guishable fermions, and therefore our trial wave functions are nodeless. The technical details of our DMC calculations are given in Appendix B 1. Binding energies for free and impurity-bound excitons and trions, in different dielectric environments, are reported in Table II.

TABLE I. Model parameters for MoSe_2 and WSe_2 , extracted from Refs. [21, 23, 32, 37, 38], and the heterobilayer $\text{MoSe}_2/\text{WSe}_2$ extracted from Refs. [10, 12, 39]. The interlayer gap \tilde{E}_g was estimated from the luminescence spectrum reported in Ref. [12], considering the exciton binding energies of Table II. From left to right, the single-layer parameters are: lattice constant a , VB and CB masses m_v and m_c , screening length r_* in a vacuum environment, and Fermi velocity γ . The heterobilayer parameters are: valence and conduction interlayer spacing Δ_v and Δ_c , interlayer band gap \tilde{E}_g , and interlayer distance d .

	a (Å)	m_v/m_0	m_c/m_0	r_* (Å)	γ (eV Å)
MoSe_2	3.30	0.44	0.38	39.79	2.53
WSe_2	3.29	0.34	0.29	45.11	3.17
	Δ_v (eV)	Δ_c (eV)	\tilde{E}_g (eV)	d (Å)	
$\text{MoSe}_2/\text{WSe}_2$	0.36	0.36	1.5	6.48	

The simplest interlayer excitonic complex is a donor-bound exciton $D_{c'}^0 h_v$, where $D_{c'}^0$ represents a positive donor ion that has been neutralized by binding an electron from band c' , and h_v a hole from band v . (When complex labels appear as subscripts in formulas, we will suppress the v and c subscripts for clarity.) DMC simulations predict that this complex is unbound due to the screening of the interlayer interaction between holes and the strongly bound neutral donor state $D_{c'}^0$, whose binding energy is $\mathcal{E}_{D^0}^b = -229.03$ meV (Table II). We therefore consider the recombination of a neutral donor $D_{c'}^0$ with delocalized holes in band v .

Adding one more electron we obtain a donor-bound trion. Alternatively, this complex can be viewed as an interlayer exciton $X_{vc'}$ bound by a neutral donor $D_{c'}^0$, leading to the notation $D_{c'}^0 X_{vc'}$. Remarkably, this larger complex is stable up to ~ 256 K, with binding energy $\mathcal{E}_{D^0 X}^b \approx 22.53$ meV (Table II) for the most energetically favorable dissociation channel into a neutral donor $D_{c'}^0$ and an interlayer exciton $X_{vc'}$.

In the following sections we calculate the photoemission rates of these two complexes using the formalism described in Sec. II.

B. $D_{c'}^0 h_v$: Neutral donor and free hole

The initial state for the recombination process of a neutral donor and a free hole is given in second quantization by

$$|D^0; \mathbf{k}_h\rangle = \frac{1}{\sqrt{S}} \sum_{\mathbf{k}} \tilde{\chi}_{\mathbf{k}} c_{c', \tau', \sigma'}^{\dagger}(\mathbf{k}) c_{v, \tau, \sigma}(\mathbf{k}_h) |\Omega\rangle, \quad (12)$$

where $\tilde{\chi}_{\mathbf{k}} = \int \chi(\mathbf{r}) e^{-i\mathbf{k} \cdot \mathbf{r}} d^2r$ is the Fourier transform of the donor-atom wave function centered at the donor site.

TABLE II. Binding energies \mathcal{E}^b of some charge-carrier complexes in a MoSe_2 monolayer, a WSe_2 monolayer, and a $\text{MoSe}_2/\text{WSe}_2$ heterobilayer in different dielectric environments including: vacuum on both sides, SiO_2 on one side and vacuum on the other, bulk hBN on one side and vacuum on the other, and bulk hBN on both sides. In the heterobilayer it is assumed that the donor ion and electrons occur in the MoSe_2 layer, while the holes are confined to the WSe_2 layer. The material parameters are listed in Table I. The DMC error bars are everywhere smaller than 0.2 meV.

System	ϵ	Binding energy (meV)			
		$X_{vc'}$	$X_{vc'c'}^-$	$D_{c'}^0$	$D_{c'}^0 X_{vc'}$
$\text{hBN}/\text{MoSe}_2/\text{hBN}$	4	194	16.2	260	21.0
$\text{hBN}/\text{WSe}_2/\text{hBN}$	4	160	13.6	215	18.1
vac./ $\text{MoSe}_2/\text{WSe}_2/\text{vac.}$	1	206	6.2	540	40.3
$\text{SiO}_2/\text{MoSe}_2/\text{WSe}_2/\text{vac.}$	2.45	123	5.1	329	30.1
$\text{hBN}/\text{MoSe}_2/\text{WSe}_2/\text{vac.}$	2.5	121	5.2	324	29.9
$\text{hBN}/\text{MoSe}_2/\text{WSe}_2/\text{hBN}$	4	84.2	4.1	229	22.5

Relative to the neutral vacuum, the state's energy can be written as $E_{D^0}(\mathbf{k}_h) = E_{c'}(0) - E_v(\mathbf{k}_h) - \mathcal{E}_{D^0}^b$, with $\mathcal{E}_{D^0}^b$ the binding energy.

In the close-alignment limit and in the absence of intervalley scattering, the complex described by Eq. (12) can decay through radiative recombination only if $\tau' = \tau$. Furthermore, spin-valley locking [37] and the known band ordering of MoSe_2 and WSe_2 monolayers [32] further require that $\sigma = \sigma'$. Considering single-photon final states of the form $|f\rangle = a_{\tau}^{\dagger}(\mathbf{q}) |\Omega\rangle$, with polarization determined by the valley quantum number, and assuming a small twist angle $\theta \approx 0^\circ$, Eqs. (10) and (11) give the radiative decay rate

$$\Gamma_{D^0 h}^< = \frac{4\tilde{E}_g}{\hbar} \frac{e^2}{\hbar c} \left[\frac{3t_{vv}\gamma'}{\hbar c \Delta_v} - \frac{3t_{cc}\gamma}{\hbar c (\Delta_c + \mathcal{E}_{D^0}^b)} \right]^2 \times \left| \int d^2r e^{i\Delta\mathbf{K} \cdot \mathbf{r}} \chi(\mathbf{r}) \right|^2 n_h, \quad (13)$$

where n_h is the hole density of the sample. To evaluate Eq. (13), we obtain the wave function $\chi(\mathbf{r})$ of the donor-bound electron by solving the two-body problem with a finite-element method, as detailed in Appendix E. Note that a finite amplitude for radiative recombination depends critically on the electron-hole asymmetry, and on having different tunneling strengths between the CBs and the VBs of the two layers, owing to the symmetry properties of the band states.

C. $D_{c'}^0 X_{vc'}$: Donor-bound interlayer trion

As discussed above, a donor-bound trion $D_{c'}^0 X_{vc'}$ can be viewed as an interlayer exciton bound to a neutral donor ion. Defining the interlayer exciton $X_{vc'}$ and $D_{c'}^0$ energies as $E_X = E_{c'}(0) - E_v(0) - \mathcal{E}_X^b$ and $E_{D^0} = E_{c'}(0) - \mathcal{E}_{D^0}^b$, respectively, the energy of a $D_{c'}^0 X_{vc'}$ complex can be expressed as $E_{D^0 X} = E_{D^0} + E_X - \mathcal{E}_{D^0 X}^b$, with $\mathcal{E}_{D^0 X}^b$ the

binding energy. Its eigenstate is given by

$$|D^0 X\rangle = \frac{1}{S^{3/2}} \sum_{\mathbf{k}_h, \mathbf{k}_1, \mathbf{k}_2} \tilde{\Phi}_{\mathbf{k}_h, \mathbf{k}_1, \mathbf{k}_2} \times c_{c', \tau', \sigma}^\dagger(\mathbf{k}_1) c_{c', -\tau', -\sigma'}^\dagger(\mathbf{k}_2) c_{v, \tau, \sigma}(\mathbf{k}_h) |\Omega\rangle, \quad (14)$$

with its two electrons belonging to opposite valleys, thus minimizing their mutual repulsion [see Eqs. (1a) and (1b)]. In this case, we consider decay into states of the form $|f\rangle = a_\tau^\dagger(\mathbf{q})|D^0\rangle$, which are energetically favorable given the large binding energies of $D_{c'}^0$ bound states. The corresponding radiative rate for close interlayer alignment is given by

$$\Gamma_{D^0 X}^< \approx \frac{4\tilde{E}_g e^2}{\hbar c} \left| \int d^2 r \int d^2 r' e^{i\Delta\mathbf{K}\cdot\mathbf{r}} \chi^*(\mathbf{r}') \Phi(\mathbf{r}, \mathbf{r}, \mathbf{r}') \right|^2 \times \left[\frac{3t_{vv}\gamma'}{\hbar c(\Delta_v + \mathcal{E}_{D^0 X}^b + \mathcal{E}_X^b)} - \frac{3t_{cc}\gamma}{\hbar c(\Delta_c + \mathcal{E}_{D^0 X}^b + \mathcal{E}_X^b)} \right]^2. \quad (15)$$

The donor atom in the final state can be in its ground state, or in any excited state allowed by angular momentum conservation. This constitutes a series of radiative subchannels, and in principle results in a series of lines with energies determined by the donor atom spectrum. The main subchannel, corresponding to the ground state $\chi_{1s}(\mathbf{r})$, produces the main emission line at $E_* = \tilde{E}_g - (\mathcal{E} + \mathcal{E}_{D^0 X}^b + \mathcal{E}_X^b)$. The first radially symmetric excited state, $\chi_{2s}(\mathbf{r})$, will produce an additional line ~ 167 meV above the main line. The overlap integrals between the ground-state donor-bound trion and the 1s and 2s neutral donor states were evaluated using VMC, and the latter was found to be two orders of magnitude smaller. We conclude that excited states can be neglected, and henceforth only the 1s subchannel will be considered. In the case of $\Delta K = 0$, the integral in Eq. (15) is given by $|\int d^2 r \int d^2 r' \chi^*(\mathbf{r}') \Phi(\mathbf{r}, \mathbf{r}, \mathbf{r}')|^2 = 1.47$ (see Appendix B 3 for details).

To summarize Sec. III, Fig. 1(b) shows the radiative rates of $D_{c'}^0 h_v$ and $D_{c'}^0 X_{vc'}$ in an hBN/MoSe₂/WSe₂/hBN heterostructure, for small twist angles. The large-angle asymptotic behavior of the radiative rate shown in Fig. 1(b) is discussed next.

IV. ASYMPTOTIC BEHAVIOR FOR LARGE INTERLAYER TWIST ANGLES

The asymptotic behavior of the radiative rate for large valley mismatch $\Delta\mathbf{K} \gtrsim 1/a_0^*$ can be obtained from a perturbative treatment of the short-range interactions Eq. (3). Let $|\Psi_0\rangle$ be an excitonic state of the Hamiltonian

$$\hat{H}_{LR} = \hat{H}_0 + \hat{U}_{\text{intra}}^< + \hat{U}_{\text{inter}}^<, \quad (16)$$

of energy E_Ψ^0 , containing the long-range approximation to the carrier-carrier and donor-carrier interaction. The interactions $\hat{U}_{\text{intra}}^<$ and $\hat{U}_{\text{inter}}^<$ are given by the expressions (8a) and (8b), respectively, with the substitutions

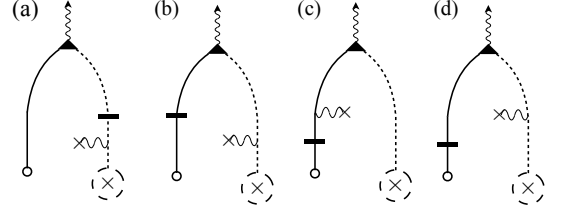


FIG. 3. Diagrams for the radiative recombination of neutral donors $D_{c'}^0$ with free holes h_v . The solid (dashed) line represents a free hole (electron); the donor impurity center is represented by a “ \times ” symbol, and the $D_{c'}^0$ state by “ \times ” in a dashed circle. Horizontal lines correspond to interlayer tunneling, wavy lines to Coulomb scattering, and the triangular vertex represents radiative recombination.

$\mathcal{V}'(\xi) \rightarrow \mathcal{V}'_<(\xi)$ and $\mathcal{W}(\xi) \rightarrow \mathcal{W}_<(\xi)$ [see Eqs. (2a) and (2b)]. The state $|\Psi_0\rangle$ is perturbed by the interlayer tunneling term \hat{H}_t , as well as the short-range interaction $\hat{U}_{\text{intra}}^>$, obtained by substituting $\mathcal{V}'(\xi) \rightarrow \mathcal{V}'_>(\xi)$ in Eq. (8a) [see Eq. (3)]. As discussed above, the short-range interlayer term is exponentially suppressed, and can be ignored altogether. As a consequence, short-range impurity scattering can take place exclusively in the electron layer (see diagrams of Fig. 3).

The momentum transfer dependence of Eq. (3) justifies treating $\hat{U}_{\text{intra}}^>$ as a perturbation. The second-order perturbative correction to the wave function relevant for photon emission is given by

$$|\Psi_0^{(2)}\rangle = \sum_{m,n} \frac{\langle n|[\hat{H}_t + \hat{U}_{\text{intra}}^>]|m\rangle \langle m|[\hat{H}_t + \hat{U}_{\text{intra}}^>]| \Psi_0 \rangle}{(E_m^0 - E_\Psi^0)(E_n^0 - E_\Psi^0)} |n\rangle, \quad (17)$$

where the sums run over the eigenstates $|n\rangle$ of \hat{H}_{LR} , with energies E_n^0 . Introducing the light-matter interaction [Eq. (9)], we focus on the diagrams of Fig. 3 for the $D_{c'}^0 h_v$ complex, and those of Fig. 4 for $D_{c'}^0 X_{vc'}$.

In general, all diagrams must be considered when evaluating the radiative decay rate. For simplicity, however, we assume that the CB and VB spacings remain the largest scales in the problem, such that $\frac{\hbar^2 \Delta K^2}{2m_\alpha} \ll \Delta_c, \Delta_v$. In this approximation, two out of the four diagrams for $D_{c'}^0 h_v$ radiative decay cancel out approximately, leaving only the contributions from the diagrams of Figs. 3(a) and (b) (see Appendix C). The resulting radiative decay rate for $D_{c'}^0 h_v$ in the large twist angle ($>$) limit is given by

$$\Gamma_{D^0 h}^> \approx \frac{64\pi^2 e^4 \tilde{E}_g}{\hbar e^2 r_*^2 \Delta K^4} \frac{e^2}{\hbar c} \left[\frac{m_{c'}}{\hbar^2 \Delta K^2} \right]^2 \left[\frac{3t_{cc}\gamma}{\hbar c \Delta_c} - \frac{3t_{vv}\gamma'}{\hbar c \Delta_v} \right]^2 \times |\chi_0(0)|^2 n_h, \quad (18)$$

where the emitted photon energy is given by $E_* = \tilde{E}_g - \mathcal{E}_{D^0}^b$. The factor of three multiplying the tunnelling amplitudes t_{cc} and t_{vv} originates from the truncated sum over reciprocal lattice vectors in Eq. (7), as a consequence of the three equivalent \mathbf{K} points in the Brillouin zone [31]. Finally, $\chi_0(\mathbf{r})$ is the $D_{c'}^0$ wave function obtained from the

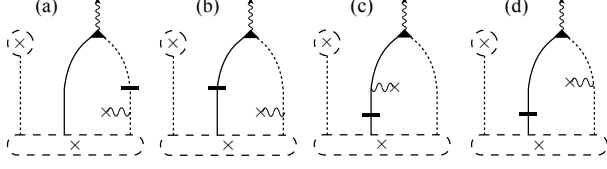


FIG. 4. Diagrams for the first radiative recombination channel of the $D_{c'}^0 X_{vc'}$ complex. The bound hole recombines with the electron from the nearest valley in the opposite layer, assisted by short-range Coulomb interactions with the donor impurity. The remaining electron stays bound to the impurity center, forming a neutral donor atom.

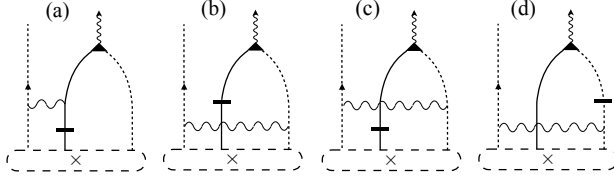


FIG. 5. Diagrams for the second radiative recombination channel of the $D_{c'}^0 X_{vc'}$ complex. The bound hole recombines with the electron from the nearest valley in the opposite layer, assisted by short-range Coulomb interactions with the second electron, at the far valley. The latter recoils and unbinds from the donor impurity.

Keldysh approximation Hamiltonian \hat{H}_{LR} , not to be confused with the full bilayer interaction bound state $\chi(\mathbf{r})$. As before, we evaluate the wave function using the finite-element method, and obtain $|\chi_0(0)|^2 = 2.678 \times 10^{-3} \text{ \AA}^{-2}$ (Appendix E).

With the perturbation $\hat{U}_{\text{intra}}^>$, there are two possible channels for radiative recombination of the $D_{c'}^0 X_{vc'}$ complex, resulting in different final states, and thus two separate lines in the PL spectrum. The first process involves one of the electrons and the hole scattering from the donor impurity and subsequently recombining, emitting a photon and leaving behind a neutral donor as the final state. This is analogous to the decay process considered in Sec. III C, and the corresponding diagrams are shown in Fig. 4. Similarly to the $D_{c'}^0 h_v$ complex case, the leading approximation to the amplitude is the sum of two diagrams, giving a radiative rate

$$\Gamma_{D^0 X}^> \approx \frac{64\pi^2 e^4 \tilde{E}_g}{\hbar e^2 r_*'^2 \Delta K^4} \frac{e^2}{\hbar c} \left[\frac{m_{c'}}{\hbar^2 \Delta K^2} \right]^2 \left[\frac{3t_{cc}\gamma}{\hbar c \Delta_c} - \frac{3t_{vv}\gamma'}{\hbar c \Delta_v} \right]^2 \times \left| \int d^2 r \chi_0^*(\mathbf{r}) \Phi_0(0, 0, \mathbf{r}) \right|^2, \quad (19)$$

where the emitted photon energy is given by $E_* = \tilde{E}_g - (\mathcal{E}_{D^0 X}^b + \mathcal{E}_X^b)$, and $\Phi_0(\mathbf{r}_h, \mathbf{r}_e, \mathbf{r}_{e'})$ is the $D_{c'}^0 X_{vc'}$ wavefunction in the Keldysh approximation.

A second radiative decay process is possible, where the recombining electron and hole scatter with the second electron, at the far valley. The latter electron recoils and is unbound from the impurity, taking some amount of kinetic energy and producing a shift in the emission line.

The corresponding diagrams are shown in Fig. 5, and give a recombination rate

$$\Gamma_{D^0 X}^> = \frac{48\pi^2 e^4 \tilde{E}_g}{\hbar e^2 r_*'^2 \Delta K^4} \frac{e^2}{\hbar c} \left[\frac{m_{c'}}{\hbar^2 \Delta K^2} \right]^2 \int d^2 r |\Phi_0(\mathbf{r}, \mathbf{r}, \mathbf{r})|^2 \times \left[\frac{t_{cc}\gamma}{\hbar c \Delta_c} - \frac{t_{vv}\gamma'}{\hbar c \Delta_v} \right]^2. \quad (20)$$

The photon energy in this case is given by $E_* = \tilde{E}_g - \mathcal{E}_{D^0 X}^b - \mathcal{E}_X^b - \frac{\hbar^2 \Delta K^2}{2m_{c'}}$, and the corresponding line in the PL spectrum is red-shifted with respect to that of the first channel by ~ 100 meV.

The overlap integrals between the initial- and final-state wave functions given in Eqs. (19) and (20) were evaluated in VMC for the Hamiltonian \hat{H}_{LR} . We obtain $|\int d^2 r \chi_0^*(\mathbf{r}) \Phi_0(0, 0, \mathbf{r})|^2 = 6.94 \times 10^{-7} \text{ \AA}^{-4}$, and $\int d^2 r |\Phi_0(\mathbf{r}, \mathbf{r}, \mathbf{r})|^2 = 3.22 \times 10^{-7} \text{ \AA}^{-4}$, respectively (see Appendix B 3).

Eqs. (18), (19) and (20) show that the radiative channels considered for the two complexes decay with the interlayer twist angle as θ^{-8} , in the limit $\Delta K \gg 1/r_*, 1/r_*'$. This is shown in Fig. 1(b) for angles larger than 6° . Our analysis indicates that, even in the case of localized impurity-bound states, the observation of photoluminescence from interlayer excitonic complexes in TMD bilayers requires near perfect alignment between the two layers.

V. PHONON-ASSISTED RECOMBINATION

Electron-phonon (e-ph) interactions introduce yet another channel for radiative recombination. Similarly to the electron recoil process discussed above, when phonons are emitted during the recombination of a given complex, they absorb part of the energy and produce a red-shifted replica in the PL spectrum. The following analysis is carried out in terms of the VMC wave functions $|\Psi\rangle$ discussed in Sec. III, evaluated with the exact bilayer interactions $\mathcal{V}'(\xi)$ and $\mathcal{W}(\xi)$.

The e-ph interaction Hamiltonian is given by

$$\hat{H}_{\text{e-ph}} = \sum_{\alpha=v,c} \sum_{\tau,\sigma} \sum_{\mathbf{k},\mathbf{q},\nu} \frac{g_{\nu,\alpha}(\mathbf{q})}{\sqrt{S}} (b_{h,\nu,-\mathbf{q}}^\dagger + b_{h,\nu,\mathbf{q}}) \times c_{\alpha,\tau,\sigma}^\dagger(\mathbf{k} + \mathbf{q}) c_{\alpha,\tau,\sigma}(\mathbf{k}) + \sum_{\alpha=v',c'} \sum_{\tau,\sigma} \sum_{\mathbf{k},\mathbf{q},\nu} \frac{g_{\nu,\alpha}(\mathbf{q})}{\sqrt{S}} (b_{e,\nu,-\mathbf{q}}^\dagger + b_{e,\nu,\mathbf{q}}) \times c_{\alpha,\tau,\sigma}^\dagger(\mathbf{k} + \mathbf{q}) c_{\alpha,\tau,\sigma}(\mathbf{k}), \quad (21)$$

where $b_{\Lambda,\nu,\mathbf{q}}^\dagger$ ($b_{\Lambda,\nu,\mathbf{q}}$) is the creation (annihilation) operator for a phonon of momentum \mathbf{q} and mode ν in the electron ($\Lambda = e$) or hole ($\Lambda = h$) layer, which couples to an electron in band $\alpha = c', v', c, v$ with strength $g_{\nu,\alpha}(\mathbf{q})$.

We consider the longitudinal optical ($\nu = \text{LO}$), homopolar ($\nu = \text{HP}$), and longitudinal acoustic ($\nu = \text{LA}$)

phonon modes allowed by the lattice symmetry. The e-ph couplings are given by

$$\begin{aligned} g_{\text{LO},\alpha}(\mathbf{q}) &= \frac{1}{A} \sqrt{\frac{\hbar}{2\rho(M_r/M)\omega_{\text{LO}}}} \frac{2\pi Z_\alpha e^2}{1 + qr_*}, \\ g_{\text{HP},\alpha}(\mathbf{q}) &= \sqrt{\frac{\hbar}{2\rho\omega_{\text{HP}}}} D_\alpha, \\ g_{\text{LA},\alpha}(\mathbf{q}) &= \sqrt{\frac{\hbar}{2\rho\omega_{\text{LA}}}} \Xi_\alpha q, \end{aligned} \quad (22)$$

where ρ is the mass density, M_r is the metal-and-two-chalcogen system reduced mass, M is the total mass of the unit cell, and A is the unit-cell area of the corresponding TMD layer. ω_ν is the phonon frequency, which we approximate as a constant for the optical modes, and as $\omega_{\text{LA}} = c_{\text{LA}} q$ for the LA mode, with c_{LA} being the sound velocity. Z is the Born effective charge, r_* is the screening length, and D_α and Ξ_α are the deformation potentials of the optical and acoustic modes, respectively. The various parameters are taken from Refs. [40–43], and summarized in Table V. We focus on the low-temperature limit, where phonon occupation is low and phonon absorption can be neglected.

Perturbative corrections to the interlayer excitonic state $|\Psi\rangle$ by the interlayer hopping and e-ph interactions are given by

$$|\Psi^{(2)}\rangle = \sum_{m,n} \frac{\langle n|[\hat{H}_t + \hat{H}_{\text{e-ph}}]|m\rangle\langle m|[\hat{H}_t + \hat{H}_{\text{e-ph}}]|\Psi\rangle}{(E_m - E_\Psi)(E_n - E_\Psi)} |n\rangle. \quad (23)$$

The relevant diagrams for radiative recombination with phonon emission are shown in Figs. 6 and 7 for $\text{D}_{c'}^0 \text{h}_v$ and $\text{D}_{c'}^0 \text{X}_{vc'}$, respectively. In both figures, panels (a)–(d) correspond to single-phonon emission in the hole layer (WSe₂), whereas panels (e)–(h) correspond to single-phonon emission in the electron layer (MoSe₂). Although in principle the two sets of diagrams give separate lines at energies determined by the phonon energy in each layer, the parameters reported in Table V show that these lines are within only a few meV of each other. For simplicity, we assume that the two layers have the same optical-phonon energies and acoustic-phonon sound velocities, producing a single line in the PL spectrum. The resulting radiative rates are given in the limit of large twist angle ($>$) by (Appendix D)

$$\begin{aligned} \Gamma_{\text{D}_{c'}^0 \text{h}_v}^{>,\nu} &\approx \frac{48\tilde{E}_g}{\hbar} \frac{e^2}{\hbar c} \left[\frac{\gamma' t_{vv}}{\hbar c \Delta_v} - \frac{\gamma t_{cc}}{\hbar c \Delta_c} \right]^2 n_{\text{h}} \\ &\times \left[\left(\frac{m_v g_{\nu,v}(\Delta K)}{\hbar^2 \Delta K^2} \right)^2 + \left(\frac{m_{c'} g_{\nu,c'}(\Delta K)}{\hbar^2 \Delta K^2} \right)^2 \right], \end{aligned} \quad (24a)$$

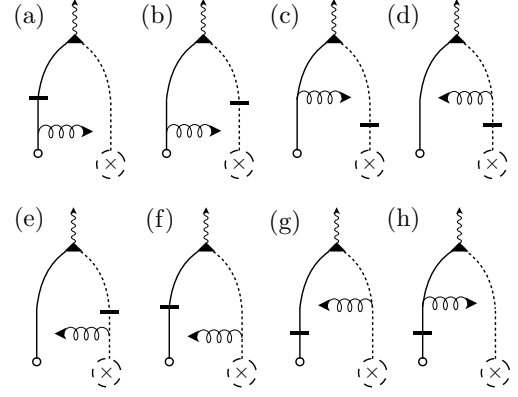


FIG. 6. Diagrams for the radiative recombination of the $\text{D}_{c'}^0 \text{h}_v$ complex with phonon scattering. The top four diagrams correspond to phonon emission in the WSe₂ layer and the bottom four diagrams correspond to phonon emission in the MoSe₂ layer.

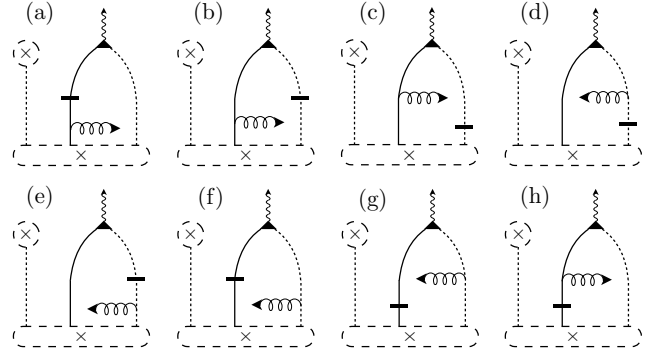


FIG. 7. Diagrams for the radiative recombination of the $\text{D}_{c'}^0 \text{X}_{vc'}$ complex with phonon scattering and $\text{D}_{c'}^0$ in the final state. The top four diagrams correspond to phonon emission in the WSe₂ layer and the bottom four diagrams correspond to phonon emission in the MoSe₂ layer.

$$\begin{aligned} \Gamma_{\text{D}_{c'}^0 \text{X}}^{>,\nu} &\approx \frac{48\tilde{E}_g}{\hbar} \frac{e^2}{\hbar c} \left[\frac{\gamma' t_{vv}}{\hbar c \Delta_v} - \frac{\gamma t_{cc}}{\hbar c \Delta_c} \right]^2 \\ &\times \left[\left(\frac{m_v g_{\nu,v}(\Delta K)}{\hbar^2 \Delta K^2} \right)^2 + \left(\frac{m_{c'} g_{\nu,c'}(\Delta K)}{\hbar^2 \Delta K^2} \right)^2 \right] \\ &\times \int d^2 r \left| \int d^2 r' \chi^*(\mathbf{r}') \Phi(\mathbf{r}, \mathbf{r}, \mathbf{r}') \right|^2. \end{aligned} \quad (24b)$$

The VMC estimate of the overlap of $\chi(\mathbf{r}')$ with $\Phi(\mathbf{r}, \mathbf{r}, \mathbf{r}')$ can be found in Table VI.

In the small-twist-angle limit ($<$), phonon emission from $\text{D}_{c'}^0 \text{h}_v$ complexes is dominated by the diagram of Fig. 6(a). In that process, the phonon is emitted by a hole in the WSe₂ layer, which then tunnels to recombine with the electron bound to the donor impurity. By contrast, all other diagrams shown in Fig. 6 involve ionization of the donor atom, which is suppressed by the large binding energy of the $\text{D}_{c'}^0$ complex. The radiative rates for $\text{D}_{c'}^0 \text{h}_v$ can thus be approximated by (Appendix

TABLE III. Electron-phonon coupling parameters for LO, HP, and LA phonon modes. ω_{LO} and ω_{HP} are the LO- and HP-mode frequencies, c_{LA} is the speed of sound for the LA mode, ρ is the mass density, D_α and Ξ_α are the deformation potentials of the optical and acoustic modes, respectively, M_r/M is the ratio of the metal-and-two-chalcogen system reduced mass to the total mass of the unit cell, and Z is the Born effective charge.

	$\hbar\omega_{\text{LO}}$ (meV)	$\hbar\omega_{\text{HP}}$ (meV)	c_{LA} (cm/s)	ρ (g/cm ³)	D_c (eV/Å)	D_v (eV/Å)	Ξ_c (eV)	Ξ_v (eV)	M_r/M	Z
MoSe ₂	37	30	4.8×10^5	4.5×10^{-7}	5.2	4.9	3.4	2.8	0.235	1.8
WSe ₂	31	31	4.4×10^5	6.1×10^{-7}	2.3	3.1	3.2	2.1	0.249	1.08

D)

$$\Gamma_{D^0 h}^{<, \nu=\text{LO/HP}} \approx \frac{6\tilde{E}_g e^2}{\pi\hbar \hbar c} \left[\frac{\gamma' t_{vv}}{\hbar c \Delta_v} \right]^2 \left[\frac{|g_{\nu, c'}(\Delta K)|^2}{(\hbar\omega_\nu + \mathcal{E}_{D^0}^b)^2} \right] \times \frac{m_v |g_{\nu, v}(\Delta K)|^2}{\hbar^3 \omega_\nu} \left| \int d^2 r e^{i\Delta \mathbf{K} \cdot \mathbf{r}} \chi(\mathbf{r}) \right|^2 n_h, \quad (25a)$$

$$\Gamma_{D^0 h}^{<, \text{LA}} \approx \frac{6\tilde{E}_g e^2}{\pi\hbar \hbar c} \frac{m_v \Xi_v^2}{\hbar^2 \rho c_{\text{LA}}^2} \left[\frac{\gamma' t_{vv}}{\hbar c \Delta_v} \right]^2 \times \left| \int d^2 r e^{i\Delta \mathbf{K} \cdot \mathbf{r}} \chi(\mathbf{r}) \right|^2 n_h. \quad (25b)$$

In the $D_{c'}^0 X_{vc'}$ case at small twist angles, the phonon emission process is suppressed by the ionization of the complex in the intermediate state and the overlap integral between the initial $D_{c'}^0 X_{vc'}$ and final $D_{c'}^0$ states. The rates are given by

$$\Gamma_{D^0 X}^{<, \nu=\text{LO/HP}} = \frac{12\tilde{E}_g e^2}{\hbar \hbar c} \frac{|g_{\nu, v}(0)|^2 + |g_{\nu, c'}(0)|^2}{(\hbar\omega_\nu + \mathcal{E}_{D^0 X}^b + \mathcal{E}_X^b)^2} \times \left[\frac{\gamma' t_{vv}}{\hbar c \Delta_v} - \frac{\gamma t_{cc}}{\hbar c \Delta_c} \right]^2 \int d^2 r \left| \int d^2 r' \chi^*(\mathbf{r}') \Phi(\mathbf{r}, \mathbf{r}, \mathbf{r}') \right|^2, \quad (26a)$$

$$\Gamma_{D^0 X}^{<, \text{LA}} = \frac{3\tilde{E}_g e^2}{\sqrt{2} \hbar^3 c_{\text{LA}}} \frac{(m_v + m_{c'})^{3/2}}{\hbar c \sqrt{\mathcal{E}_{D^0 X}^b + \mathcal{E}_X^b}} \left[\frac{\gamma' t_{vv}}{\hbar c \Delta_v} - \frac{\gamma t_{cc}}{\hbar c \Delta_c} \right]^2 \times \left[\frac{\Xi_v^2}{\rho} \left| \int d^2 r \int d^2 r' e^{-i\Delta \mathbf{K} \cdot \mathbf{r}} \chi^*(\mathbf{r}') \Phi(\mathbf{r}, \mathbf{r}, \mathbf{r}') \right|^2 + \frac{\Xi_{c'}^2}{\rho'} \left| \int d^2 r \int d^2 r' e^{i\Delta \mathbf{K} \cdot \mathbf{r}} \chi^*(\mathbf{r}') \Phi(\mathbf{r}, \mathbf{r}, \mathbf{r}') \right|^2 \right], \quad (26b)$$

where ρ and ρ' are the mass densities of WSe₂ and MoSe₂, respectively (Table V).

Eqs. (24a)–(26b) contain a factor of three originating from the tunnelling process, which gives three distinct intermediate states with different emitted phonon wave vectors, related by C_3 symmetry. As a result, the interference leading to the factor of nine in the interaction-driven processes of Secs. III and IV is absent in this case.

Additional contributions to the LO phonon emission come from e-ph interaction of a carrier in one layer with an LO phonon in the other. This is made possible by the long range of the LO phonon-induced potential. The

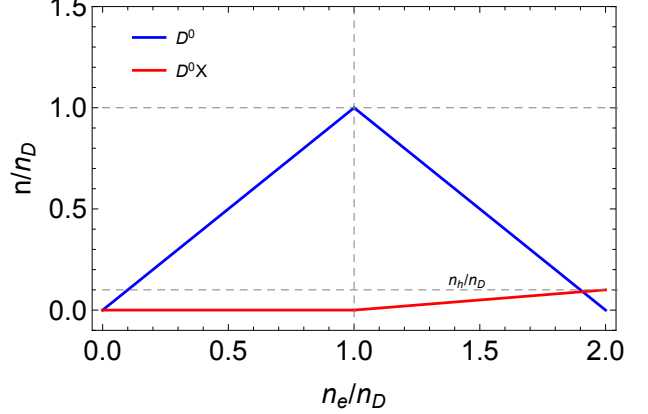


FIG. 8. Model for the density of complexes $D_{c'}^0$ and $D_{c'}^0 X_{vc'}$ as a function of the electron density n_e .

interlayer separation results in an exponential suppression of the potential in the interlayer distance and momentum transfer as $e^{-\Delta K d}$, which nonetheless is approximately unity in the limit of close alignment. Thus, we add this contribution to the LO-phonon-assisted recombination rates for $D_{c'}^0 h_v$ and $D_{c'}^0 X_{vc'}$ complexes in the small-twist-angle limit.

The total phonon emission rates for the two complexes, combining the three phonon modes, are shown in Fig. 1(b) as functions of the twist angle. As mentioned above, the phonon contribution to the recombination rate is most significant for the $D_{c'}^0 h_v$ complex, being an order of magnitude larger than for $D_{c'}^0 X_{vc'}$. The LO phonon mode in the hole layer (WSe₂) is the dominant phonon-assisted process overall, and gives a significant decay rate in the small-twist-angle limit. As a result, we predict additional phonon replica lines in the PL spectrum, red-shifted by the phonon energy $\hbar\omega_{\text{LO}} = 31$ meV with respect to the main $D_{c'}^0 h_v$ and $D_{c'}^0 X_{vc'}$ lines. The $D_{c'}^0 h_v$ phonon replica line gives the most dominant feature, with decay rates comparable to the main $D_{c'}^0 h_v$ line.

VI. INTENSITY DEPENDENCE ON DOPING

In addition to the decay rates, the relative line intensities also depend on the distribution of $D_{c'}^0 h$ and $D_{c'}^0 X_{vc'}$ complexes in the system. At charge neutrality, neutral excitonic complexes such as $D_{c'}^0 h_v$ are energetically favorable, whereas additional electrons introduced into the sample will bind to existing neutral donors to form $D_{c'}^0 X_{vc'}$ complexes. Thus the relative population of

complexes can be controlled through doping.

In this section we model the evolution of the PL spectrum with the carrier density. We assume a constant density n_h of laser-pumped holes and a large density of donor impurities in the sample, and consider the tuning of the electron density n_e by electrostatic gating [18]. Under these assumptions, and given that the net population of donor-bound complexes is limited by the donor density n_D , we limit our discussion to the regime where $n_h \ll n_e \sim n_D$.

We use a simplified zero-temperature model for the occupations of the two complexes, shown in Fig. 8. There are two main regimes determined by the sample-dependent donor density n_D . In the p-doped regime, defined by $0 < n_e < n_D$, added electrons neutralize the excess positive donors, forming $D_{c'}^0$ complexes that can recombine with the optically pumped holes. In this regime, the formation of $D_{c'}^0 X_{vc'}$ complexes is energetically unfavorable, and thus thermally suppressed until all donors have been neutralized.

By contrast, in the n-doped regime, defined by $n_D < n_e < 2n_D$, it is energetically favorable for additional electrons to bind with an existing neutral donor to form either a charged donor state $D_{c'c'}^-$ (Table IV), or a donor-bound trion $D_{c'}^0 X_{vc'}$. For the latter case we must consider that laser-pumped holes are scarce ($n_h \ll n_D$), and thus the probability of forming a $D_{c'}^0 X_{vc'}$ complex will be proportional to n_h/n_D . The increase in electron density is accompanied by a decrease in $D_{c'}^0 h_v$ numbers, and a much slower increase in the $D_{c'}^0 X_{vc'}$ population, until the number of donor-bound trions in the system equals the number of available holes. This is shown in Fig. 8.

The line intensities within this model are given by

$$I_{D^0h} \approx \Gamma_{D^0h} \begin{cases} n_e, & n_e < n_D \\ n_D \left[1 - \frac{n_e - n_D}{n_D} \right], & n_D < n_e < 2n_D \end{cases}, \quad (27)$$

and

$$I_{D^0X} \approx \Gamma_{D^0X} \begin{cases} 0, & n_e < n_D \\ n_D \frac{n_h}{n_D} \frac{n_e - n_D}{n_D}, & n_D < n_e < 2n_D \end{cases}. \quad (28)$$

The resulting simulated PL spectrum is shown in Fig. 9 for different doping densities, given in terms of the donor density in the MoSe₂ layer. A Gaussian lineshape was used for the lines with an experimentally motivated broadening [18] of $2\sigma = 60$ meV. The spectrum shows the three dominant lines, $D_{c'}^0 h_v$, $D_{c'}^0 X_{vc'}$, and the red-shifted phonon replica of $D_{c'}^0 h_v$, with the lines' peak energies determined by the DMC-obtained binding energies. The three complexes evolve with doping as prescribed by the occupation model [Eqs. (27) and (28)]. The $D_{c'}^0 h_v$ complex and its phonon replica dominate at low doping, but the $D_{c'}^0 X_{vc'}$ complex grows slowly in intensity with increasing doping, leading to a simultaneous reduction in the intensity of the $D_{c'}^0 h_v$ complex. For the broadening used in the simulated PL spectrum, the proximity of the three lines results in an intricate line form, providing a signature in PL experiments for the intrinsic structure of the interlayer emission line.

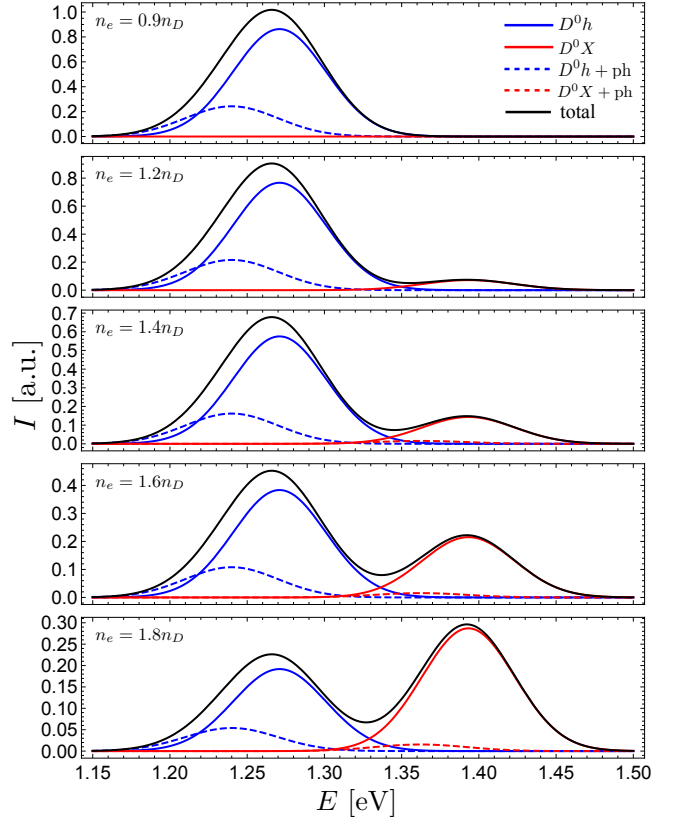


FIG. 9. Simulated normalized PL spectra for a closely aligned ($\theta \approx 0^\circ$) MoSe₂/WSe₂ heterobilayer, originating from the $D_{c'}^0 h_v$ and $D_{c'}^0 X_{vc'}$ complexes at different electron densities n_e , given in terms of the fixed donor density n_D . Dashed curves correspond to the phonon replicas. The lines are assumed to have Gaussian shapes of width $2\sigma = 60$ meV, and we use $n_h = 10^{11} \text{ cm}^{-2}$ and $n_D = 10^{13} \text{ cm}^{-2}$.

VII. CONCLUSIONS

The momentum mismatch between twisted and incommensurate heterobilayer TMDs prevents efficient radiative recombination of interlayer complexes composed of electrons and holes localized on opposite layers. In this paper we have provided a mechanism to bridge the momentum gap involving donor impurities present in the heterobilayer system, both at small and large twist angles. The donor impurities were found to provide deep potential wells (~ 200 meV), resulting in strongly bound interlayer complexes, as revealed by DMC calculations. Focusing on the simplest multiparticle complexes, we obtain radiative rates of up to a few μs^{-1} for the neutral donor with a free hole $D_{c'}^0 h_v$ and the donor-bound trion $D_{c'}^0 X_{vc'}$ complexes for closely aligned layers, and a strong twist-angle suppression for large misalignment with the asymptotic form $\propto \theta^{-8}$. A comparable contribution was found for the $D_{c'}^0 h_v$ complex from emission of optical phonons, resulting in a total of three dominant and doping-tunable lines in the PL spectrum. The $D_{c'}^0 h_v$ and its phonon replica are expected to dominate the emission spectrum for electron densities below the sample-dependent donor concentration; conversely, PL

from the $D_{c'}^0 X_{vc'}$ complex is expected to dominate the interlayer sector of the spectrum when the electron density exceeds the density of donors.

ACKNOWLEDGMENTS

M.D., D.A.R-T., and V.I.F. wish to thank F. Vialla and F. Koppens for fruitful discussions. M.D., D.A.R-T., and V.I.F. acknowledge support from ERC Syn-

ergy Grant Hetero2D, EPSRC EP/N010345, EPSRC EP/P026850/1, Lloyd Register Foundation Nanotechnology grant, and support from the European Graphene Flagship Project. R.J.H. is fully funded by the Graphene NOWNANO centre for doctoral training (EPSRC grant no. EP/L01548X/1). M.S. was funded by the EPSRC standard grant “Non-perturbative and stochastic approaches to many-body localization” (Grant No. EP/P010180/1). Computer time was provided by Lancaster University’s High-End Computing facility, and we have also made use of the N8 HPC – funded by the N8 consortium and the EPSRC (Grant No. EP/K000225/1).

[1] A. K. Geim and I. V. Grigorieva, *Nature* **499**, 419 (2013).

[2] K. S. Novoselov, A. Mishchenko, A. Carvalho, and A. H. Castro Neto, *Science* **353**, aac9439 (2016).

[3] W. Zhang, Q. Wang, Y. Chen, Z. Wang, and A. T. S. Wee, *2D Mater.* **3**, 022001 (2016).

[4] M. M. Furchi, A. Pospischil, F. Libisch, J. Burgdörfer, and T. Mueller, *Nano Letters* **14**, 4785 (2014).

[5] C.-H. Lee, G.-H. Lee, A. M. van der Zande, W. Chen, Y. Li, M. Han, X. Cui, G. Arefe, C. Nuckolls, T. F. Heinz, J. Guo, J. Hone, and P. Kim, *Nature Nanotechnology* **9**, 676 EP (2014).

[6] M. Szyniszewski, E. Mostaani, N. D. Drummond, and V. I. Fal’ko, *Phys. Rev. B* **95**, 081301 (2017).

[7] A. T. Hanbicki, M. Currie, G. Kioseoglou, A. L. Friedman, and B. T. Jonker, *Solid State Commun.* **203**, 16 (2015).

[8] T. Cao, G. Wang, W. Han, H. Ye, C. Zhu, J. Shi, Q. Niu, P. Tan, E. Wang, B. Liu, and J. Feng, *Nat. Commun.* **3**, 887 (2012).

[9] X. Xu, W. Yao, D. Xiao, and T. F. Heinz, *Nat. Phys.* **10**, 343 (2014).

[10] C. Gong, H. Zhang, W. Wang, L. Colombo, R. M. Wallace, and K. Cho, *Appl. Phys. Lett.* **103**, 053513 (2013).

[11] J. Kang, S. Tongay, J. Zhou, J. Li, and J. Wu, *Appl. Phys. Lett.* **102**, 012111 (2013).

[12] P. Rivera, J. R. Schaibley, A. M. Jones, J. S. Ross, S. Wu, G. Aivazian, P. Klement, K. Seyler, G. Clark, N. J. Ghimire, J. Yan, D. G. Mandrus, W. Yao, and X. Xu, *Nat. Commun.* **6**, 6242 (2015).

[13] P. Nagler, G. Plechinger, M. V. Ballottin, A. Mitioglu, S. Meier, N. Paradiso, C. Strunk, A. Chernikov, P. C. M. Christianen, C. Schüller, and T. Korn, *2D Mater.* **4**, 025112 (2017).

[14] E. M. Alexeev, A. Catanzaro, O. V. Skrypka, P. K. Nayak, S. Ahn, S. Pak, J. Lee, J. I. Sohn, K. S. Novoselov, H. S. Shin, and A. I. Tartakovskii, *Nano Letters* **17**, 5342 (2017), <https://doi.org/10.1021/acs.nanolett.7b01763>.

[15] H. Yu, Y. Wang, Q. Tong, X. Xu, and W. Yao, *Phys. Rev. Lett.* **115**, 187002 (2015).

[16] D. M. Ceperley and B. J. Alder, *Phys. Rev. Lett.* **45**, 566 (1980).

[17] W. M. C. Foulkes, L. Mitas, R. J. Needs, and G. Rajagopal, *Rev. Mod. Phys.* **73**, 33 (2001).

[18] F. Vialla and F. Koppens, (2017), (private communication).

[19] L. V. Keldysh, *J. Exp. Theor. Phys.* **29**, 658 (1979).

[20] B. Ganchev, N. Drummond, I. Aleiner, and V. Fal’ko, *Phys. Rev. Lett.* **114**, 107401 (2015).

[21] T. C. Berkelbach, M. S. Hybertsen, and D. R. Reichman, *Phys. Rev. B* **88**, 045318 (2013).

[22] M. Van der Donck, M. Zarenia, and F. M. Peeters, *Phys. Rev. B* **96**, 035131 (2017).

[23] E. Mostaani, M. Szyniszewski, C. H. Price, R. Maezono, M. Danovich, R. J. Hunt, N. D. Drummond, and V. I. Fal’ko, *Phys. Rev. B* **96**, 075431 (2017).

[24] A. Ramasubramaniam, *Phys. Rev. B* **86**, 115409 (2012).

[25] K. F. Mak, K. He, C. Lee, G. H. Lee, J. Hone, T. F. Heinz, and J. Shan, *Nature Materials* **12**, 207 EP (2012).

[26] J. S. Ross, S. Wu, H. Yu, N. J. Ghimire, A. M. Jones, G. Aivazian, J. Yan, D. G. Mandrus, D. Xiao, W. Yao, and X. Xu, *Nat. Commun.* **4**, 1474 EP (2013).

[27] Y. Lin, X. Ling, L. Yu, S. Huang, A. L. Hsu, Y.-H. Lee, J. Kong, M. S. Dresselhaus, and T. Palacios, *Nano Letters* **14**, 5569 (2014), <http://dx.doi.org/10.1021/nl501988y>.

[28] Y. Yu, S. Hu, L. Su, L. Huang, Y. Liu, Z. Jin, A. A. Purezky, D. B. Geohegan, K. W. Kim, Y. Zhang, and L. Cao, *Nano Letters* **15**, 486 (2015), <http://dx.doi.org/10.1021/nl5038177>.

[29] H. Wang, C. Zhang, W. Chan, C. Manolatou, S. Tiwari, and F. Rana, *Phys. Rev. B* **93**, 045407 (2016).

[30] M. Koshino and P. Moon, *J. Phys. Soc. Jpn.* **84**, 121001 (2015).

[31] Y. Wang, Z. Wang, W. Yao, G.-B. Liu, and H. Yu, *Phys. Rev. B* **95**, 115429 (2017).

[32] A. Kormányos, G. Burkard, M. Gmitra, J. Fabian, V. Zólyomi, N. D. Drummond, and V. Fal’ko, *2D Mater.* **2**, 022001 (2015).

[33] R. Geick, C. H. Perry, and G. Rupprecht, *Phys. Rev.* **146**, 543 (1966).

[34] M. F. Plass, W. Fukarek, A. Kolitsch, N. Schell, and W. Möller, *Thin Solid Films* **305**, 172 (1997).

[35] K.-L. Barth, W. Fukarek, H.-P. Maucher, M. F. Plass, and A. Lunk, *Thin Solid Films* **313**, 697 (1998).

[36] S. L. Rumyantsev, M. E. Levinshtein, A. D. Jackson, S. N. Mohammad, G. L. Harris, M. G. Spencer, and M. Shur, in *Properties of Advanced Semiconductor Materials GaN, AlN, InN, BN, SiC, SiGe*, edited by M. E. Levinshtein, S. L. Rumyantsev, and M. S. Shur (John Wiley & Sons New York, NY, USA, 2001) Chap. 4, pp. 67–92.

[37] D. Xiao, G.-B. Liu, W. Feng, X. Xu, and W. Yao, *Phys. Rev. Lett.* **108**, 196802 (2012).

[38] A. Kumar and P. Ahluwalia, *Physica B: Condens. Matter* **407**, 4627 (2012).

[39] B. Amin, N. Singh, and U. Schwingenschlögl, *Phys. Rev. B* **92**, 075439 (2015).

- [40] M. Danovich, I. L. Aleiner, N. D. Drummond, and V. I. Fal'ko, IEEE J. Sel. Top. Quantum Electron. **23**, 168 (2017).
- [41] Z. Jin, X. Li, J. T. Mullen, and K. W. Kim, Phys. Rev. B **90**, 045422 (2014).
- [42] X. Gu and R. Yang, Appl. Phys. Lett. **105**, 131903 (2014).
- [43] K. Kaasbjerg, K. S. Thygesen, and A.-P. Jauho, Phys. Rev. B **87**, 235312 (2013).
- [44] H. Ogata, Publ. Res. Inst. Math. Sci. **41**, 949 (2005).
- [45] N. D. Drummond, M. D. Towler, and R. J. Needs, Phys. Rev. B **70**, 235119 (2004).
- [46] P. López Ríos, P. Seth, N. D. Drummond, and R. J. Needs, Phys. Rev. E **86**, 036703 (2012).
- [47] T. Kato, Comm. Pure Appl. Math. **10**, 151 (1957).
- [48] C. J. Umrigar, K. G. Wilson, and J. W. Wilkins, Phys. Rev. Lett. **60**, 1719 (1988).
- [49] N. D. Drummond and R. J. Needs, Phys. Rev. B **72**, 085124 (2005).
- [50] C. J. Umrigar, J. Toulouse, C. Filippi, S. Sorella, and R. G. Hennig, Phys. Rev. Lett. **98**, 110201 (2007).
- [51] R. J. Needs, M. D. Towler, N. D. Drummond, and P. López Ríos, J. Phys. Condens. Matter **22**, 023201 (2010).
- [52] *Mathematica, Version 11.0.1* (Wolfram Research, Inc., Champaign, Illinois, U.S.A., 2016).

Appendix A: Long-range interaction between charge carriers

1. Multilayer Keldysh interaction

Consider a vdW heterostructure of 2D semiconductors comprised of N parallel layers (labelled $i = \{1, 2, \dots, N\}$), each having in-plane susceptibility κ_i and z -coordinate d_i . Suppose this heterostructure is immersed in an isotropic medium of dielectric constant ϵ . In practice the dielectric constant is taken to be the average of the dielectric constants of the media above and below the heterobilayer.

Suppose that a test charge density

$$\rho_{\text{tot}}^j(\mathbf{r}, z) = \rho^j(\mathbf{r})\delta(z - d_j), \quad (\text{A1})$$

is present in layer j . The resulting electric displacement field is

$$\mathbf{D} = -\frac{\epsilon}{4\pi}\nabla\phi(\mathbf{r}, z) - \sum_i \kappa_i[\nabla_{\parallel}\phi(\mathbf{r}, d_i)]\delta(z - d_i), \quad (\text{A2})$$

where ∇_{\parallel} is the 2D gradient operator (excluding the z -component). Gauss's law yields

$$\begin{aligned} \rho^j(\mathbf{r}, z)\delta(z - d_j) &= -\frac{\epsilon}{4\pi}\nabla^2\phi(\mathbf{r}, z) \\ &\quad - \sum_i \kappa_i[\nabla_{\parallel}^2\phi(\mathbf{r}, d_i)]\delta(z - d_i). \end{aligned} \quad (\text{A3})$$

Taking the Fourier transform gives

$$\rho^j(\mathbf{q})e^{-ikd_j} = \frac{\epsilon}{4\pi}(q^2 + k^2)\phi(\mathbf{q}, k) + q^2 \sum_i \kappa_i\phi(\mathbf{q}, d_i)e^{-ikd_i}, \quad (\text{A4})$$

which, after Fourier inversion in the k variable only, gives

$$\rho^j(\mathbf{q})e^{-q|z-d_j|} = \frac{\epsilon}{2\pi}q\phi(\mathbf{q}, z) + q^2 \sum_i \kappa_i\phi(\mathbf{q}, d_i)e^{-q|z-d_i|}. \quad (\text{A5})$$

Evaluating Eq. (A5) at each layer ($z = d_l$, $l = \{1, 2, \dots, N\}$), we find

$$\begin{aligned} \rho^j e^{-q|d_l - d_j|} &= q[\epsilon/(2\pi) - \kappa_l q]\phi(\mathbf{q}, d_l) \\ &\quad + q^2 \sum_{i \neq l} \kappa_i\phi(\mathbf{q}, d_i)e^{-q|d_l - d_i|}, \end{aligned} \quad (\text{A6})$$

which is a matrix equation

$$\rho_l^j(\mathbf{q}) = \sum_i M_{li}(\mathbf{q})\phi_i(\mathbf{q}), \quad (\text{A7})$$

where

$$\begin{aligned} \rho_l^j(\mathbf{q}) &= \rho^j(\mathbf{q})e^{-q|d_l - d_j|}, \\ \phi_l(\mathbf{q}) &= \phi(\mathbf{q}, d_l), \\ M_{li} &= \begin{cases} q[\epsilon/(2\pi) + \kappa_l q] & \text{if } i = l \\ q^2\kappa_i e^{-q|d_l - d_i|} & \text{otherwise} \end{cases}. \end{aligned} \quad (\text{A8})$$

The solution to Eq. (A7) is a set of $\phi_i(\mathbf{q}) \equiv \rho^j(\mathbf{q}) \times v_{ji}(\mathbf{q})$, with $v_{ji}(\mathbf{q})$ being the Fourier components of the interaction potential between layer j and layer i . If $j = i$ then this is the intralayer interaction in layer j . This procedure should, in general, be repeated for $j = 1, 2, \dots, N$; however, if there is sufficient symmetry (e.g., a mirror symmetry about a plane through the center of the heterostructure) then only a subset of j values will require explicit solution of Eq. (A7).

The same analysis applies in the case that the surrounding dielectric medium is anisotropic, having dielectric tensor

$$\tilde{\epsilon} = \begin{pmatrix} \epsilon_{\parallel} & 0 & 0 \\ 0 & \epsilon_{\parallel} & 0 \\ 0 & 0 & \epsilon_{\perp} \end{pmatrix}, \quad (\text{A9})$$

provided the substitutions

$$d \rightarrow D = \sqrt{\epsilon_{\parallel}/\epsilon_{\perp}}d, \quad (\text{A10})$$

$$\epsilon \rightarrow \bar{\epsilon} = \sqrt{\epsilon_{\parallel}\epsilon_{\perp}}, \quad (\text{A11})$$

are also made.

2. Numerical evaluation of the bilayer Keldysh interaction

In the bilayer case ($N = 2$), it is straightforward to solve Eq. (A7) to obtain the intra- (\mathcal{V} and \mathcal{V}') and interlayer (\mathcal{W}) potentials of Eqs. (1a)–(1c).

Continuum QMC calculations require the potential energy to be evaluated in real space. We therefore require the inverse Fourier transforms of Eqs. (1a)–(1c), which reduce to Hankel transforms due to the circular symmetry of the interaction potentials.

At long range (small q), the intralayer interaction $\mathcal{V}(\mathbf{q}) = 2\pi/\{\epsilon q[1 + (r_* + r'_*)q]\} + O(q)$ reduces to the monolayer Keldysh form [19], with an effective screening length $r_*^{\text{eff}} = r_* + r'_*$. The inverse Fourier transform can be performed analytically in this limit, giving

$$\begin{aligned} \mathcal{V}(r) \approx & \frac{\pi}{2\epsilon(r_* + r'_*)} \\ & \times [H_0(r/(r_* + r'_*)) - Y_0(r/(r_* + r'_*))] \\ & + O(r^{-3}), \end{aligned} \quad (\text{A12})$$

where H_0 and Y_0 are a Struve function and a Bessel function of the second kind, respectively. Equation (A12) is a good approximation at long range.

At short range (large q), the intralayer interaction of Eq. (1a) again reduces to the monolayer Keldysh form, but this time with $r_*^{\text{eff}} = r_*$, i.e., the second layer becomes irrelevant. On the other hand, at very long range, the monolayer Keldysh interaction is also valid, since $\mathcal{V}(\mathbf{q}) = 2\pi/(\epsilon q) + O(1)$ at small q so that the interaction is of Coulomb form. Thus the monolayer Keldysh interaction

$$\mathcal{V}(r) \approx \frac{\pi}{2\epsilon r_*^{\text{eff}}} [H_0(r/r_*^{\text{eff}}) - Y_0(r/r_*^{\text{eff}})] + O(r^{-2}), \quad (\text{A13})$$

is a reasonable approximation to the intralayer interaction at *both* short and very long range.

To evaluate the “full” intralayer interaction numerically, we used the quadrature method of Ogata [44] to perform the Hankel transform of $\mathcal{V}(\mathbf{q}) - 2\pi/\{\epsilon q[1 + r_* q]\}$, then added the result to the monolayer Keldysh interaction of Eq. (A13). Partitioning the interaction into a long-range part and a numerically evaluated short-range part ensures that the quadrature is relatively straightforward, and that we can introduce a cutoff at large r , beyond which the numerical corrective term is negligible.

At small q , the interlayer interaction of Eq. (1c) reduces to the displaced Coulomb form $\mathcal{W}(q) = 2\pi e^{-(r_* + r'_* + d)q}/(\epsilon q) + O(q)$; hence the long-range interlayer potential in real space is given by

$$\mathcal{W}(r) \approx \frac{1}{4\pi\sqrt{r^2 + (r_* + r'_* + d)^2}} + O(r^{-3}). \quad (\text{A14})$$

At short range in real space the interlayer interaction should be nondivergent. Equation (A14) satisfies this qualitative requirement.

To evaluate the “full” interlayer interaction numerically, we performed the numerical Hankel transform of $\mathcal{W}(\mathbf{q}) - 2\pi e^{-(r_* + r'_* + d)q}/(\epsilon q)$, then added the result to Eq. (A14).

There is an alternative long-range approximation to the interlayer potential, which is more like the intralayer potential. Noting that $\mathcal{W}(\mathbf{q}) = 2\pi/\{\epsilon q[1 + (r_* + r'_* + d)q]\} + O(q)$, the long-range interlayer potential reduces to a Keldysh potential with $r_*^{\text{eff}} = r_* + r'_* + d$, giving

$$\begin{aligned} \mathcal{W}(r) \approx & \frac{\pi}{2\epsilon(r_* + r'_* + d)} \\ & \times \left[H_0\left(\frac{r}{r_* + r'_* + d}\right) - Y_0\left(\frac{r}{r_* + r'_* + d}\right) \right] \\ & + O(r^{-3}). \end{aligned} \quad (\text{A15})$$

This introduces unphysical singular behavior into the interlayer interaction at short range.

Appendix B: QMC calculations

1. Technical details

We performed VMC and DMC calculations [16, 17] for complexes of distinguishable charge carriers and fixed ions interacting via the “full” bilayer potential [Eqs. (1a)–(1c)] and the approximate small- q Keldysh form of the potential [Eqs. (A12) and (A15)], as described in Appendix A 2. We used trial wave functions of Jastrow form, where the Jastrow exponents contained smoothly truncated polynomial particle-particle terms, ion-particle terms, ion-particle-particle, and particle-particle-particle terms [45, 46]. Additional terms satisfying the analogs of the Kato cusp conditions [6, 20, 47] were applied to the trial wave function between pairs of particles wherever there was a logarithmic divergence in the interaction between them, including the unphysical divergences in the approximate Keldysh interaction. Free parameters were optimized using VMC with variance [48, 49] and energy minimization [50] as implemented in the CASINO code [51].

In our DMC calculations we used two DMC time steps in the ratio 1:4 and corresponding target populations in the ratio 4:1, allowing a simultaneous extrapolation to zero time step and infinite population. Since the charge carriers are distinguishable, there is no fixed-node error and hence DMC provides exact ground-state solutions to the effective-mass model of interacting charge carriers with the chosen model interaction.

2. Energies of complexes in the hBN/MoSe₂/WSe₂/hBN heterostructure

Table IV shows the resulting total energies of complexes in the hBN/MoSe₂/WSe₂/hBN heterostructure. For completeness we include results in which the electrons are found in either layer; however, the results of immediate relevance to this paper are those for which the electrons are all found in the MoSe₂ layer. DMC results for two-particle complexes were found to agree with calculations performed using Mathematica’s finite-element method [52] (see Appendix E). Using total energies, one can assess the most energetically favorable dissociations (see Table V) and therefore calculate binding energies of various complexes.

It is clear from Table V that the approximate Keldysh interaction performs well at calculating binding energies provided the dissociation does not involve significant changes to short-range pair distributions. As an extreme case, the binding energy of an exciton, which is simply equal to its total energy and hence does not benefit from any cancellation of errors, is overestimated by 23% when the approximate Keldysh interaction is used.

TABLE IV. Total DMC energies of various charge-carrier complexes in the hBN/MoSe₂/WSe₂/hBN heterostructure calculated using the Keldysh approximation to the bilayer potential [Eqs. (A12) and (A15)] and the full bilayer interaction [Eqs. (1a)–(1c)]. Primes (') indicate that a charge carrier is in the MoSe₂ layer; otherwise the charge carrier is in the WSe₂ layer. Donor charges are always assumed to be in the MoSe₂ layer. The subscripts *c* and *v* indicate whether charge carriers are electrons (*c*) or holes (*v*).

Complex	DMC total energy (meV)	
Approx.	Keldysh	Bilayer potential
X _{vc'}	-103.958669(5)	-84.232(1)
D _{c'} ⁰	-163.2478711(5)	-229.03306(1)
X _{vc'c'} ⁻	-108.1967(4)	-88.32(3)
D _{c'c'} ⁻	-176.9426(3)	-249.60(2)
D _{c'c'} ⁰ h _v	-163.4819(8)	-
D _{c'c'} ⁰ X _{vc'}	-278.73(2)	-335.781(4)
D _{c'c'} ⁻ X _{vc'}	-292.83(1)	-
X _{vc}	-114.601814(1)	-140.4303329(4)
D _c ⁰	-124.890219(9)	-102.5996(7)
X _{vc'c'} ⁻	-120.6018(5)	-
X _{vc'c'} ⁻	-123.7189(5)	-152.25(1)
D _{cc'} ⁻	-165.8499(5)	-
D _{cc'} ⁻	-129.3199(9)	-
D _{c'c'} ⁺ X _{vc}	-133.758(2)	-141.716(8)
D _{c'c'} ⁰ X _{vc}	-279.776(5)	-
D _{c'c'} ⁻ X _{vc}	-301.81(1)	-
D _{c'c'} ⁰ X _{vc'c'} ⁻	-295.00(1)	-

TABLE V. Dissociations of complexes and the associated binding energies in hBN/MoSe₂/WSe₂/hBN. The naming convention for the carrier complexes is explained in the caption of Table IV.

Dissociation process	Binding energy (meV)	
Approx.	Keldysh	Bilayer pot.
X _{vc'c'} ⁻ → X _{vc'} + e _{c'}	4.2380(4)	4.09(3)
D _{c'c'} X _{vc'} → X _{vc'} + D _{c'} ⁰	11.52(2)	22.516(4)
D _{c'c'} X _{vc'} → X _{vc'} + D _{c'c'} ⁻	11.93(1)	-
D _{c'c'} ⁻ → D _{c'} ⁰ + e _{c'}	13.6948(3)	20.57(1)
D _{c'c'} ⁰ h _v → D _{c'} ⁰ + h _v	0.2340(8)	-
X _{vc'c'} ⁻ → X _{vc} + e _{c'}	6.0000(5)	< 0
X _{vc'c'} ⁻ → X _v + e _c	9.1170(5)	11.83(1)
D _{c'c'} X _{vc} → X _{vc} + D _{c'} ⁰	1.926(5)	-
D _{c'c'} X _{vc} → X _{vc} + D _{c'c'} ⁻	10.26(1)	-
D _{cc'} ⁻ → D _{c'} ⁰ + e _c	2.6020(5)	-
D _{c'c'} X _{vc'c'} ⁻ → D _{c'} ⁰ + X _{vc'}	8.03(1)	-
D _{cc'} ⁻ → D _{c'} ⁰ + e _c	4.4297(9)	< 0
D _{c'c'} ⁺ X _{vc} → D _{c'} ⁺ + X _{vc}	19.156(2)	1.286(8)

3. Calculation of the overlap integrals

a. VMC evaluation of the normalization integral of a many-body wave function

Consider a complex of *N* quantum particles with unnormalized wave function $\Phi(\mathbf{R})$, where $\mathbf{R} = (\mathbf{r}_1, \dots, \mathbf{r}_N)$ is the $2N$ -dimensional vector of all particle coordinates. Let $\Psi(\mathbf{R})$ be a normalized, bound-state sampling wave function, which ideally has a large overlap with Φ and

the same asymptotic behavior. Then

$$\int |\Phi(\mathbf{R})|^2 d^{2N} \mathbf{R} = \int |\Psi(\mathbf{R})|^2 \left| \frac{\Phi(\mathbf{R})}{\Psi(\mathbf{R})} \right|^2 d^{2N} \mathbf{R} = \left\langle \left| \frac{\Phi(\mathbf{R})}{\Psi(\mathbf{R})} \right|^2 \right\rangle_{|\Psi|^2}. \quad (\text{B1})$$

Hence we can evaluate the normalization of Φ by VMC sampling of $|\Psi(\mathbf{R})|^2$. We used the simple Jastrow form

$$\Psi(\mathbf{R}) = \prod_{i=1}^N \left(\sqrt{\frac{2}{\pi}} ce^{-cr_i} \right), \quad (\text{B2})$$

for the sampling wave function, where the exponent *c* is a positive, adjustable parameter that was chosen to maximize the efficiency of the calculation.

b. Evaluation of overlap integrals

Numerical estimates of the various overlap integrals in the expressions for the radiative recombination rates of donor-bound trions in a hBN/MoSe₂/WSe₂/hBN system are reported in Table VI. The ground state $\chi_{1s}(\mathbf{r}_e)$ and the first excited state $\chi_{2s}(\mathbf{r}_e)$ of the neutral donor atom ($D_{c'}^0$) were calculated using a finite-element method (see Appendix E). Using a VMC-optimized trial wave function $\Phi(\mathbf{r}_h, \mathbf{r}_{e_1}, \mathbf{r}_{e_2})$ for the ground state of the donor-bound negative trion ($D_{c'}^0 X_{vc'}$), we employed a grid-based method to evaluate those overlap integrals in Table VI that can be reduced to one-dimensional radial integrals. The remaining integrals were evaluated by a VMC method, as described below.

Let Ψ be a sampling wave function, as defined in Appendix B 3 a. The overlap of the trion wave function with the donor-atom wave function when an electron and a hole are pinned vertically above one another is

$$\begin{aligned} & \int \int \chi^*(\mathbf{r}_1) \Phi(\mathbf{r}_2, \mathbf{r}_2, \mathbf{r}_1) d^2 \mathbf{r}_1 d^2 \mathbf{r}_2 \\ &= \int |\Psi(\mathbf{R})|^2 \frac{\chi^*(\mathbf{r}_2) \Phi(\mathbf{r}_1, \mathbf{r}_2, \mathbf{r}_1)}{|\Psi(\mathbf{R})|^2} d^4 \mathbf{R} \\ &= \left\langle \frac{\chi^*(\mathbf{r}_2) \Phi(\mathbf{r}_1, \mathbf{r}_2, \mathbf{r}_1)}{|\Psi(\mathbf{R})|^2} \right\rangle_{|\Psi|^2}. \end{aligned} \quad (\text{B3})$$

The last expression can readily be evaluated by VMC sampling of $|\Psi|^2$, using accurate numerical representations of the donor-atom wave function $\chi(\mathbf{r}_e)$ obtained in the finite-element calculations.

The overlap integrals are accurate to at least three significant figures; however there is an unknown error arising from the fact that the trial wave function $\Phi(\mathbf{r}_h, \mathbf{r}_{e_1}, \mathbf{r}_{e_2})$ only approximates the exact ground state.

Appendix C: Radiative recombination assisted by short-range Coulomb interactions

Consider the wave function $\chi(\mathbf{r})$ for $D_{c'}^0$ complexes in the long-range (Keldysh) approximation described in Sec.

TABLE VI. Overlap integrals required for calculations of radiative recombination rates. Calculations are performed for a hBN/MoSe₂/WSe₂/hBN system. $\Phi(\mathbf{r}_h, \mathbf{r}_{e1}, \mathbf{r}_{e2})$ is the ground-state wave function of the donor-bound negative trion, with both donor and electrons in the MoSe₂ layer and the hole in the WSe₂ layer ($D_c^0 X_{vc'}$). $\chi_{1s}(\mathbf{r}_e)$ and $\chi_{2s}(\mathbf{r}_e)$ are the ground-state and first-excited-state (rotationally invariant) wave functions of the neutral donor atom in the MoSe₂ layer (D_c^0).

Overlap	Approx.	Keldysh	Bilayer pot.
$\frac{ \Phi(\mathbf{0}, \mathbf{0}, \mathbf{0}) ^2}{\int \Phi ^2 d^6 \mathbf{R}}$		$1.29 \times 10^{-9} \text{ \AA}^{-6}$	$2.75 \times 10^{-9} \text{ \AA}^{-6}$
$\frac{\int \Phi(\mathbf{r}, \mathbf{r}, \mathbf{0}) d^2 \mathbf{r}}{\int \Phi ^2 d^6 \mathbf{R}}$		$8.09 \times 10^{-3} \text{ \AA}^{-2}$	$6.08 \times 10^{-3} \text{ \AA}^{-2}$
$\frac{\int \Phi(\mathbf{r}, \mathbf{r}, \mathbf{0}) ^2 d^2 \mathbf{r}}{\int \Phi ^2 d^6 \mathbf{R}}$		$1.28 \times 10^{-6} \text{ \AA}^{-4}$	$1.38 \times 10^{-6} \text{ \AA}^{-4}$
$\frac{\int \Phi(\mathbf{r}, \mathbf{r}, \mathbf{r}) ^2 d^2 \mathbf{r}}{\int \Phi ^2 d^6 \mathbf{R}}$		$3.22 \times 10^{-7} \text{ \AA}^{-4}$	$2.37 \times 10^{-7} \text{ \AA}^{-4}$
$\frac{\int \chi_{1s}(\mathbf{r}) \Phi(\mathbf{0}, \mathbf{0}, \mathbf{r}) ^2 d^2 \mathbf{r}}{\int \Phi ^2 d^6 \mathbf{R} \times \int \chi_{1s} ^2 d^2 \mathbf{r}}$		$6.94 \times 10^{-7} \text{ \AA}^{-4}$	$1.21 \times 10^{-6} \text{ \AA}^{-4}$
$\frac{\int \int \chi_{1s}(\mathbf{r}') \Phi(\mathbf{r}, \mathbf{r}, \mathbf{r}') d^2 \mathbf{r} d^2 \mathbf{r}'}{\int \Phi ^2 d^6 \mathbf{R} \times \int \chi_{1s} ^2 d^2 \mathbf{r}}$	3.54		1.47
$\frac{\int \int \chi_{1s}(\mathbf{r}') \Phi(\mathbf{r}, \mathbf{r}, \mathbf{r}') d^2 \mathbf{r}' d^2 \mathbf{r}'}{\int \Phi ^2 d^6 \mathbf{R} \times \int \chi_{1s} ^2 d^2 \mathbf{r}}$		$5.90 \times 10^{-4} \text{ \AA}^{-2}$	$3.85 \times 10^{-4} \text{ \AA}^{-2}$
$\frac{\int \chi_{2s}(\mathbf{r}) \Phi(\mathbf{0}, \mathbf{0}, \mathbf{r}) d^2 \mathbf{r}}{\int \Phi ^2 d^6 \mathbf{R} \times \int \chi_{2s} ^2 d^2 \mathbf{r}}$		$2.01 \times 10^{-8} \text{ \AA}^{-4}$	$1.13 \times 10^{-7} \text{ \AA}^{-4}$
$\frac{\int \int \chi_{2s}(\mathbf{r}') \Phi(\mathbf{r}, \mathbf{r}, \mathbf{r}') d^2 \mathbf{r} d^2 \mathbf{r}'}{\int \Phi ^2 d^6 \mathbf{R} \times \int \chi_{2s} ^2 d^2 \mathbf{r}}$	0.0379		0.0254
$\frac{\int \int \chi_{2s}(\mathbf{r}') \Phi(\mathbf{r}, \mathbf{r}, \mathbf{r}') d^2 \mathbf{r}' d^2 \mathbf{r}'}{\int \Phi ^2 d^6 \mathbf{R} \times \int \chi_{2s} ^2 d^2 \mathbf{r}}$		$1.04 \times 10^{-5} \text{ \AA}^{-2}$	$1.89 \times 10^{-5} \text{ \AA}^{-2}$

IV. The complex state can be written in the form of Eq. (12), with the substitution $\tilde{\chi}_{\mathbf{k}} \rightarrow \tilde{\chi}_{\mathbf{k}}^0$, and short-range electrostatic interactions and interlayer tunneling can be treated as perturbations to this initial state. Setting $\tau' = \tau$ and $\sigma' = \sigma$ in Eq. (12), radiative decay is determined by the matrix element $\langle \tau, \mathbf{q} | \hat{H}_r | D^0; \mathbf{k}_h \rangle^{(2)}$, where $|\tau, \mathbf{q}\rangle = a_{\tau}^{\dagger}(\mathbf{q}) |\Omega\rangle$ is the final state in which a photon of momentum \mathbf{q} and the appropriate polarization τ has been emitted after recombination of the bound electron with the delocalized hole. The notation $|A\rangle^{(2)}$ indicates that the state includes corrections up to second order in perturbation theory, in this case from the interlayer tunneling (\hat{H}_t) and short-range interaction ($\hat{U}_{\text{intra}}^>$) terms.

The diagrams of Fig. 3 correspond to those corrections to the wave function that are relevant for radiative recombination in the large-twist-angle regime, where $\mathcal{E}_{D^0}^b \ll \frac{\hbar^2 \Delta K^2}{2m_{\alpha}}$. Following the order of the diagrams in the figure, and assuming that $k_h, q \ll \Delta K$, the optical matrix element for $D_c^0 h_v$ recombination is given in terms of the real-space impurity wave function by

$$\langle \tau, \mathbf{q} | \hat{H}_r | D^0; \mathbf{k}_h \rangle^{(2)} = \left[-\frac{\gamma t_{cc}/\hbar c}{(\mathcal{E}_{D^0}^b + \Delta_c) \left(\mathcal{E}_{D^0}^b + \frac{\hbar^2 \Delta K^2}{2m_{c'}} \right)} + \frac{\gamma' t_{vv}/\hbar c}{\left(\mathcal{E}_{D^0}^b + \Delta_v + \frac{\hbar^2 \Delta K^2}{2m_{c'}} + \frac{\hbar^2 \Delta K^2}{2m_{v'}} \right) \left(\mathcal{E}_{D^0}^b + \frac{\hbar^2 \Delta K^2}{2m_{c'}} \right)} \right. \\ \left. - \frac{\gamma' t_{vv}/\hbar c}{\Delta_v \left(\Delta_v + \frac{\hbar^2 \Delta K^2}{2m_{v'}} \right)} + \frac{\gamma' t_{vv}/\hbar c}{\left(\mathcal{E}_{D^0}^b + \Delta_v + \frac{\hbar^2 \Delta K^2}{2m_{c'}} + \frac{\hbar^2 \Delta K^2}{2m_{v'}} \right) \left(\Delta_v + \frac{\hbar^2 \Delta K^2}{2m_{v'}} \right)} \right] \frac{6\pi e^3 \chi(0)}{\epsilon r_*' S \Delta K^2} \sqrt{\frac{4\pi \hbar c}{L \sqrt{q_{\perp}^2 + q_{\parallel}^2}}}, \quad (C1)$$

We additionally assume that the CB and VB spacings remain a large scale in the problem, such that $\frac{\hbar^2 \Delta K^2}{2m_{\alpha}} \ll \Delta_c, \Delta_v$. In this approximation, the third and fourth terms in Eq. (C1) cancel out, corresponding to diagrams Fig. 3(c) and (d). Substituting the resulting expression into Eq. (11) gives Eq. (18), where the probability that the hole state is occupied is introduced through the hole density $N(\mathbf{k}_h)$. This analysis can be carried out for $D_c^0 X_{vc'}$ complexes, yielding Eqs. (19) and (20).

The large momentum components introduced by the short-range interaction terms are irrelevant in the small-twist-angle regime, which is dominated by the small momentum sector of the wave function. In this case, the optical matrix element is obtained from the perturbed state $|D^0; \mathbf{k}_h\rangle^{(1)}$, including first-order tunneling correc-

tions [Eq. (10)]. The optical matrix element is

$$\langle \tau, \mathbf{q} | \hat{H}_r | D^0; \mathbf{k}_h \rangle = \frac{1}{\sqrt{S}} \int d^2 r e^{i(\Delta \mathbf{K} + \mathbf{k}_h + \mathbf{q}) \cdot \mathbf{r}} \chi(\mathbf{r}) \\ \times \sqrt{\frac{4\pi \hbar c e^2}{S L q}} \left[\frac{3t_{vv}\gamma'}{\hbar c \Delta_v} - \frac{3t_{cc}\gamma}{\hbar c (\Delta_c + \mathcal{E}_{D^0}^b)} \right]. \quad (C2)$$

Substituting into Eq. (11) leads to Eq. (13), and similar procedures are used to obtain Eq. (15) for $D_c^0 X_{vc'}$ complexes. Notice that the second radiative channel for $D_c^0 X_{vc'}$ discussed in the main text does not apply to this regime. The small-twist-angle analogue to the recoil process due to electron-electron interactions involves a small momentum transfer, and is thus already contained in the unperturbed state $|D^0 X\rangle$.

Appendix D: Phonon effects on radiative recombination

The discussion of Appendix C can easily be adapted to e-ph interactions, $\hat{H}_{\text{e-ph}}$ [Eq. (21)]. In the following we adopt the assumptions introduced in Appendix C; namely, $\frac{\hbar^2 \Delta K^2}{2m_\alpha} \ll \mathcal{E}_{\text{D}^0}^b \ll \Delta_c, \Delta_v$. In addition, we use $\hbar\omega_{\Lambda,\nu}(\xi) \ll \Delta_c, \Delta_v$, which is always valid in our cases of interest.

In the large-twist-angle regime, consider the process whereby the electron in a D_c^0 layer bridges the valley mismatch by emitting a phonon in mode ν and momentum ξ , with $\xi \sim \Delta\mathbf{K}$, in either the electron ($\Lambda = \text{e}$) or hole ($\Lambda = \text{h}$) layer. The electron recombines with a delocalized hole of momentum \mathbf{k}_h , emitting a photon of momentum \mathbf{q} and polarization μ , leading to the final state

$$\langle \tau, \mathbf{q}; \nu, \xi | \hat{H}_r | \text{D}^0; \mathbf{k}_h \rangle = a_\tau^\dagger(\mathbf{q}) b_{\Lambda, \nu, -\xi}^\dagger | \Omega \rangle. \quad (\text{D1})$$

Considering the phonon energies presented in Table V, in this regime we have $\frac{\hbar^2 \Delta K^2}{2m_\alpha} \gg \hbar\omega_{\Lambda,\nu}$, and the radiative matrix elements with phonon emission can be approximated by

$$\begin{aligned} \text{h} \langle \tau, \mathbf{q}; \nu, \xi | \hat{H}_r | \text{D}^0; \mathbf{k}_h \rangle &\approx \frac{\tilde{\chi}(\mathbf{k}_h + \xi - \Delta\mathbf{K})}{S} g_{v,\nu}(\Delta K) \\ &\times \sqrt{\frac{4\pi\hbar c}{SLq}} \frac{\gamma' t_{vv}}{\hbar c \Delta_v} \left[\frac{6m_v}{\hbar^2 \Delta K^2} - \frac{6m_{c'}}{\hbar^2 \Delta K^2} \right], \end{aligned} \quad (\text{D2a})$$

$$\begin{aligned} \text{e} \langle \tau, \mathbf{q}; \nu, \xi | \hat{H}_r | \text{D}^0; \mathbf{k}_h \rangle &\approx \frac{\tilde{\chi}(\mathbf{k}_h + \xi - \Delta\mathbf{K})}{S} g_{c',\nu}(\Delta K) \\ &\times \sqrt{\frac{4\pi\hbar c}{SLq}} \frac{\gamma t_{cc}}{\hbar c \Delta_c} \left[\frac{6m_{c'}}{\hbar^2 \Delta K^2} - \frac{6m_v}{\hbar^2 \Delta K^2} \right]. \end{aligned} \quad (\text{D2b})$$

The distinct final states lead to two independent (noninterfering) contributions to the radiative decay rate, obtained by substituting Eqs. (D2a) and (D2b) into Eq. (11). The result is Eq. (24a), and a similar procedure leads to Eq. (24b) for the phonon-assisted decay of $\text{D}_c^0 \text{X}_{vc'}$ complexes.

The situation is more subtle in the small-twist-angle regime, where $\hbar\omega_{\Lambda,\nu} \lesssim \hbar^2 \Delta K^2 / (2m_\alpha)$, and the phonon dispersion becomes important. The optical matrix elements are

$$\begin{aligned} \text{h} \langle \tau, \mathbf{q}; \xi, \nu | \hat{H}_r | \text{D}^0; \mathbf{k}_h \rangle &\approx \frac{\tilde{\chi}(\mathbf{k} + \xi - \Delta\mathbf{K})}{S} g_{v,\nu}(\xi) \\ &\times \sqrt{\frac{4\pi\hbar c}{SLq}} \left[\frac{3\gamma' t_{vv}}{\hbar c \Delta_v \left(\frac{\hbar^2 \xi^2}{2m_v} + \hbar\omega_\nu(\xi) \right)} \right. \\ &\left. - \frac{3\gamma t_{cc}}{\hbar c \Delta_c \left(\frac{\hbar^2 \xi^2}{2m_v} + \hbar\omega_\nu(\xi) + \mathcal{E}_{\text{D}^0}^b \right)} \right], \end{aligned} \quad (\text{D3})$$

$$\begin{aligned} \text{e} \langle \tau, \mathbf{q}; \xi, \nu | \hat{H}_r | \text{D}^0; \mathbf{k}_h \rangle &= \sqrt{\frac{4\pi\hbar c}{SLq}} \frac{\tilde{\chi}(\mathbf{k} + \xi - \Delta\mathbf{K})}{S} \\ &\times \left[\frac{3\gamma t_{cc} g_{\nu,c'}(\xi)}{\hbar c \Delta_c (\hbar\omega_\nu(\xi) + \mathcal{E}_{\text{D}^0}^b)} - \frac{3\gamma' t_{vv} g_{\nu,c'}(\xi)}{\hbar c \Delta_v (\hbar\omega_\nu(\xi) + \mathcal{E}_{\text{D}^0}^b)} \right]. \end{aligned} \quad (\text{D4})$$

Following Ref. [31], we use $t_{cc} \ll t_{vv}$ to simplify these expressions. Using Fermi's golden rule and integrating over the photon momentum we obtain the decay rates

$$\begin{aligned} \Gamma_{\text{D}^0 \text{h}}^{<,\nu} &\approx \sum_{\xi} \left[\frac{|g_{v,\nu}(0)|^2}{\left(\frac{\hbar^2 \xi^2}{2m_v} + \hbar\omega_\nu \right)^2} + \frac{|g_{c',\nu}(0)|^2}{(\hbar\omega_\nu + \mathcal{E}_{\text{D}^0}^b)^2} \right] \\ &\times \int d^2 r \int d^2 r' e^{i(\xi - \Delta\mathbf{K}) \cdot (\mathbf{r}' - \mathbf{r})} \chi(\mathbf{r}) \chi^*(\mathbf{r}') \\ &\times \frac{e^2}{\hbar c} \frac{12 \tilde{E}_g n_h}{\hbar S} \left[\frac{\gamma' t_{vv}}{\hbar c \Delta_v} \right]^2; \quad \nu = \text{LO, HP}, \end{aligned} \quad (\text{D5a})$$

$$\begin{aligned} \Gamma_{\text{D}^0 \text{h}}^{<,\text{LA}} &\approx \sum_{\xi} \left[\frac{|g_{v,\text{LA}}(\xi)|^2}{\left(\frac{\hbar^2 \xi^2}{2m_v} + \hbar c_{\text{LA}} \xi \right)^2} + \frac{|g_{c',\text{LA}}(\xi)|^2}{\mathcal{E}_{\text{D}^0}^b \xi^2} \right] \\ &\times \int d^2 r \int d^2 r' e^{i\xi \cdot (\mathbf{r}' - \mathbf{r})} \chi(\mathbf{r}) \chi^*(\mathbf{r}') \\ &\times \frac{e^2}{\hbar c} \frac{12 \tilde{E}_g n_h}{\hbar S} \left[\frac{\gamma' t_{vv}}{\hbar c \Delta_v} \right]^2, \end{aligned} \quad (\text{D5b})$$

for optical and acoustic phonon modes, respectively.

The divergence at $\xi = 0$ in Eq. (D5b) makes the first term dominant in the sum over ξ , and we can neglect the second. The sum can be evaluated exactly in the continuous limit. Defining $\mathcal{F}(x) = -x[Y_1(x) + H_{-1}(x)]$, where $H_n(x)$ and $Y_n(x)$ are the n th Struve function and Bessel function of the second kind, respectively, we obtain

$$\begin{aligned} \Gamma_{\text{D}^0 \text{h}}^{<,\text{LA}} &\approx \frac{e^2}{\hbar c} \frac{3\Xi_v^2 \tilde{E}_g m_v n_h}{\hbar^3 \rho c_{\text{LA}}^2} \left[\frac{\gamma' t_{vv}}{\hbar c \Delta_v} \right]^2 \\ &\times \int d^2 r \int d^2 r' e^{i\xi \cdot (\mathbf{r}' - \mathbf{r})} \chi(\mathbf{r}) \chi^*(\mathbf{r}') \mathcal{F} \left(\frac{2m_v \hbar c_{\text{LA}} |\mathbf{r}' - \mathbf{r}|}{\hbar^2} \right). \end{aligned} \quad (\text{D6})$$

From the values reported in Table V we find that the function \mathcal{F} in the integrand decays over a characteristic length scale of 100 nm, much greater than the spread of the localized wave function $\chi(\mathbf{r})$. Therefore, to a good approximation, we can substitute $\mathcal{F}(0) = 2/\pi$ to evaluate the integral. The final results for all phonon modes considered in Eqs. (25a) and (25b), and Eqs. (26a) and (26b) are obtained by a similar procedure.

Appendix E: Finite-element calculation of two body states in heterobilayer system

The Schrödinger equation for two particles interacting through a radially symmetric potential $\mathcal{U}(r)$ is given by

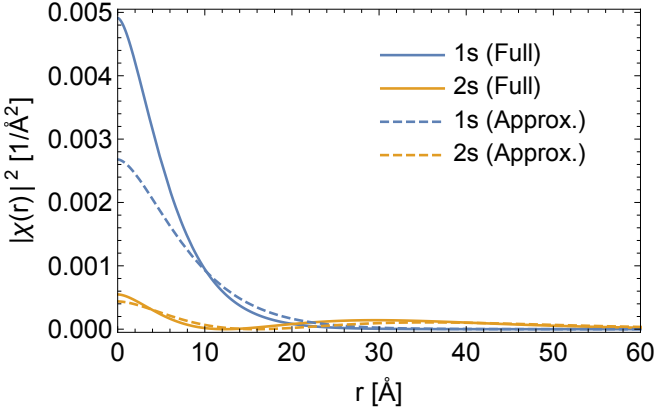


FIG. 10. Probability distributions ($|\chi(r)|^2$) of the first two radially symmetric donor atom states in hBN/MoSe₂/WSe₂/hBN. The solid lines were obtained using the full bilayer potential Eq. (1a), and correspond to states with binding energies $\mathcal{E}_{1s}^b = -229.03$ meV and $\mathcal{E}_{2s}^b = -61.73$ meV. The dashed lines were obtained using the approximate intralayer Keldysh form Eq. (A12).

[6],

$$\left[-\frac{\hbar^2}{2m_1} \nabla_e^2 - \frac{\hbar^2}{2m_2} \nabla_h^2 - e^2 \mathcal{U}(r_{12}) \right] \Psi = E \Psi, \quad (\text{E1})$$

where the form of the interaction \mathcal{U} between charge carriers is explained in Appendix A 2, depending on the layer in which each particle is found.

Transforming the coordinates to the relative motion $\mathbf{r} = \mathbf{r}_1 - \mathbf{r}_2$ and the center-of-mass motion $\mathbf{R} = \frac{m_1 \mathbf{r}_1 + m_2 \mathbf{r}_2}{m_1 + m_2}$ allows separation of the Schrödinger equation to the center-of-mass part whose solution is given by the plane wave $\phi(R) = \frac{1}{\sqrt{S}} e^{i\mathbf{K} \cdot \mathbf{R}}$ and the energy $E = \frac{\hbar^2 K^2}{2(m_1 + m_2)}$, and the relative-motion part given by

$$\left[-\frac{\hbar^2}{2\mu} \nabla^2 - e^2 \mathcal{U}(r) \right] \Psi = E \Psi, \quad (\text{E2})$$

where $\mu = m_1 m_2 / (m_1 + m_2)$ is the reduced mass.

Transforming the equation into dimensionless quantities [6, 23] using the excitonic Bohr radius $a_0^* = \frac{\epsilon \hbar^2}{\mu e^2}$ and the excitonic Rydberg energy $R_y^* = \frac{\mu e^4}{2\epsilon^2 \hbar^2}$ gives

$$\left[-\tilde{\nabla}^2 - \frac{1}{R_y^*} \mathcal{U}(a_0^* \tilde{r}) \right] \Psi = \tilde{E} \Psi. \quad (\text{E3})$$

where $\tilde{r} = r/a_0^*$ and $\tilde{E} = E/R_y^*$. Using separation of variables the general solution is given by

$$\Psi(\mathbf{r}) = R(r) \Phi(\phi), \quad (\text{E4})$$

where the angular part solution is

$$\Phi(\phi) = \frac{1}{\sqrt{2\pi}} e^{il\phi}. \quad (\text{E5})$$

$l = 0, \pm 1, \pm 2, \dots$ is the azimuthal quantum number with $\Phi(\phi)$ being an eigenfunction of the angular momentum operator $L_z = -i\hbar \frac{\partial}{\partial \phi}$ with eigenvalue $\hbar l$. The equation for the radial part is

$$-R''(\tilde{r}) - \frac{1}{\tilde{r}} R'(\tilde{r}) + \frac{l^2}{\tilde{r}^2} R(\tilde{r}) - \tilde{v}(\tilde{r}) R(\tilde{r}) = \tilde{E} R(\tilde{r}), \quad (\text{E6})$$

where $\tilde{v}(\tilde{r}) = \mathcal{U}(a_0^* \tilde{r})/R_y^*$. To solve Eq. (E6) numerically we use the substitution $u(\tilde{r}) = R(\tilde{r})\tilde{r}$, allowing us to impose Dirichlet boundary conditions: $u(\tilde{r}) = 0$ at $\tilde{r} = 0$ and $\tilde{r} = \infty$. The equation can be solved using the finite-element method implemented in Mathematica [52]. For the charged donor interacting with an electron in the MoSe₂ layer, we have $\mu = m'_c$, and we solve Eq. (E6) using both the approximate Keldysh interaction and the full bilayer potential for the intralayer interaction between the donor and electron. The normalized probability distributions for the first two radially symmetric states (1s, 2s) obtained using both potentials are plotted in Fig. 10.